UC Santa Barbara
UC Santa Barbara Electronic Theses and Dissertations

Title

Growth and Characterization of Materials and Structures for Quantum Computing

Permalink

https://escholarship.org/uc/item/2nm9t2wg

Author

Chatterjee, Shirshendu

Publication Date

2024

Peer reviewed|Thesis/dissertation

eScholarship.org Powered by the California Digital Library
University of California

University of California
Santa Barbara

Growth and Characterization of Materials and Structures for Quantum Computing

A thesis submitted in partial satisfaction
of the requirements for the degree

Master of Science
in
Electrical and Computer Engineering

by

Shirshendu Chatterjee

Committee in charge:

Professor Chris J. Palmstrøm, Chair
Professor Galan Moody
Professor Jon Schuller

June 2024

The Thesis of Shirshendu Chatterjee is approved.

Professor Galan Moody

Professor Jon Schuller

Professor Chris J. Palmstrøm, Committee Chair

June 2024

Growth and Characterization of Materials and Structures for Quantum Computing

Copyright © 2024

by

Shirshendu Chatterjee

Acknowledgements

I would like to express my heartfelt gratitude to my family, friends, and coworkers for their unwavering support. Special thanks to my advisor, Prof. Chris Palmstrøm, who not only taught me the intricacies of research but also inspired me to broaden my horizons and deepen my thinking. I am particularly grateful to Connor Dempsey, whose guidance was invaluable in both the theoretical and experimental aspects of my project. His partnership greatly enhanced my understanding and skills. Additionally, I extend my appreciation to Teun van Schijndel for his assistance and support during challenging times in the lab.

Abstract

Growth and Characterization of Materials and Structures for Quantum Computing

by

Shirshendu Chatterjee

This thesis focuses on the growth and characterization of compounds, devices, and structures for applications in Quantum computing. Quantum computing leverages the principles of quantum mechanics to process information, promising exponential speedup for certain problems. Here, we are interested in two branches - Superconducting and Topological Quantum Computing. Superconducting quantum computing uses circuits cooled to near absolute zero to create and manipulate qubits with high fidelity. Topological quantum computing, on the other hand, exploits the properties of quasiparticles called anyons to form qubits that are inherently resistant to errors, offering the potential for more stable and scalable quantum systems.

Motivated by recent advancements highlighting Ta as a promising material in low-loss superconducting circuits and showing long coherence times in superconducting qubits, we have chosen Tantalum as the superconductor. Here, we have explored the possibility of growth of Ta/Ta_2O_5/Ta Josephson Junctions for transmon qubits. The growth of such junctions was done at low temperatures using the LT-MBE.

Topological insulators can be used in topological quantum computing by exploiting their edge states, which are protected by time-reversal symmetry and are predicted to be robust against local perturbations. This protection reduces the error rates in quantum computations, enhancing the stability and coherence of qubits. Here, we demonstrate the growth of α-Sn on InSb(001) in ultrathin limit using tensile strain which is a potential topological insulator. The films were characterized electrically in a cryogenic setup using

a Hall bar geometry. Fabrication of the hall bars using low-temperature processing techniques has also been demonstrated which ensures there is no phase transition from α to β-Sn.

Contents

Abstract **v**

1 Introduction **1**
1.1 Quantum Computing . . . 1
1.2 Topological Insulators . . . 3
1.3 Superconducting Quantum Computing . . . 7
1.4 Outline of the Thesis . . . 12

2 Growth and Characterization Techniques **13**
2.1 The Palmstrøm Molecular Beam Epitaxy System . . . 13
2.2 Molecular Beam Epitaxy . . . 14
2.3 Electron Transport Characterizations . . . 17

3 In-situ growth of Josephson-Junctions for Transmon Qubits **22**
3.1 Introduction . . . 22
3.2 Shadow Masks Layout for in-situ growth . . . 23
3.3 Fabrication Methodologies . . . 24
3.4 Growth of the Ta/Ta_2O_5/Ta Josephson Junctions. . . . 28
3.5 Results and Discussion . . . 34
3.6 Conclusion . . . 37

4 α-Sn for Topological Quantum Computing. **38**
4.1 Introduction . . . 38
4.2 Growth of α-$Sn_{1-x}Ge_x$ on InSb . . . 41
4.3 Fabrication of Hall Bars . . . 44
4.4 Results and Discussion . . . 52
4.5 Conclusion . . . 59

5 Summary and Outlook **60**

A Fabrication Recipe - Shadow Mask **62**
A.1 Front Side Patterning 62
A.2 Backside Patterning 63

Bibliography **65**

Chapter 1

Introduction

1.1 Quantum Computing

Over the past century, advancements in physics have significantly influenced society and presented new challenges. Since their inception in 1947, transistors have become foundational to modern computing, making a world devoid of chips and computers unimaginable today. Although tremendous strides have been made to enhance computing capabilities, there are impending limitations related to size and power. While Moore's law predicts an exponential growth in the number of transistors per chip, quantum mechanical effects are beginning to disrupt these classical computing processes. [1]

Despite advancements in computing, solving highly complex problems often requires significant assumptions. This is particularly true in fields such as quantum chemistry, where modeling many-body systems, or in materials science, where discovering new parameters for materials like room-temperature superconductors, remains challenging. Additionally, there is room for enhancement in securing data transfers through encryption. Quantum mechanics, specifically quantum computing, holds promise in addressing these challenges. Quantum computing utilizes principles like superposition and entanglement,

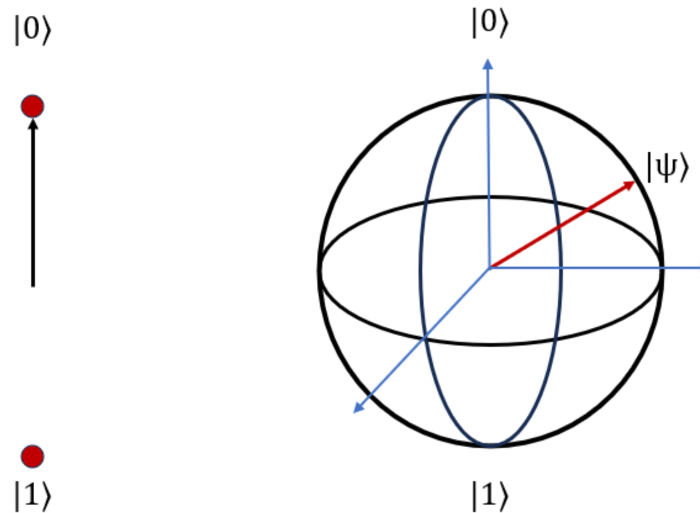

Figure 1.1: **Representation of a classical bit and a qubit.** *The classical bit only has 2 defined states, 0 and 1, while the qubit can be defined by any superposition on the sphere in between the states* $|0\rangle$ *and* $|1\rangle$*.*

providing groundbreaking methods for data processing.

In general, classical computing is based on two defined states in which a bit system can be, 0 and 1. Combining millions of these 'bits' on silicon chips with the two states enables processing sequentially through calculations and manipulations. In contrast to this deterministic behavior of classical computing, quantum computing is fundamentally different. Instead of having two determined states, a quantum bit or qubit can be a superposition of two states. Suppose the states,$|0\rangle$ and $|1\rangle$ can be in a superposition. These states can be described by the wave function $|\psi\rangle$

$$|\psi\rangle = \alpha|0\rangle + \beta|1\rangle \tag{1.1}$$

where α and β represent the amplitude of the quantum states. According to quantum mechanics, the probability of finding the state $|0\rangle$ and $|1\rangle$ are $|\alpha|^2$ and $|\beta|^2$, respectively

such that,

$$|\alpha|^2 + |\beta|^2 = 1 \quad (1.2)$$

A representation of the classical bit and quantum bit is shown in Figure 1.1.

By increasing the number of qubits in a system, the state of n qubits can exist in a superposition of all 2^n possible classical states. This superposition enables certain operations and algorithms to leverage "quantum parallelism" where the final state incorporates results from running an operation on all possible classical outcomes simultaneously. [2] The potential for massive computations with computers containing thousands of qubits makes the field of quantum computing incredibly exciting for numerous applications.

In this thesis, two branches of Quantum Computing is discussed - Topological Quantum Computing and Superconducting Quantum Computing.

1.2 Topological Insulators

Attempts to understand the phases of matter and their potential technological applications highlight our current grasp of modern quantum mechanics and its potential to drive societal progress. One such advancement is the topological insulator, a new phase of matter that stands on the boundary between insulation and conductance. This innovation could ultimately lead to the creation of quantum computers, groundbreaking devices that utilize the dynamics of atomic-scale objects for information storage and manipulation.

The story of the topological insulator began with the discovery of the quantum spin Hall effect (QSH) in 1980 [3]. The QSH effect was the first instance of a quantum state exhibiting spontaneously broken symmetry, characterized by a symmetric probability distribution where any pair of outcomes has an equal likelihood of occurring. In a paper

published in Nature [4], it was observed that this behavior depends on the topology, or the physically continuous geometric structure, of a material and its geometry at the quantum level. An example of the QSH effect occurs when a strong magnetic field is applied to a two-dimensional electron gas in a semiconductor. At low temperatures and high magnetic fields, electrons move along different regions at the edge of the semiconductor. In contrast, at normal temperatures, they remain scattered across the surface. This separation of electrons into distinct regions imparts unique properties to the material, enabling it to simultaneously conduct and insulate.

A topological insulator is essentially a hybrid between an insulator and a conductor, allowing conduction on its surface while maintaining insulation beneath it. Dr. Charles Kane and Dr. Eugene Mele from the University of Pennsylvania have been pivotal in demonstrating how the QSH state can be realized in certain theoretical models [5]. They revealed that spin-orbit coupling, an effect where electrons retain their angular momentum or rotational motion due to geometric symmetry within the material, plays a crucial role. Additionally, this coupling induces a force on electrons moving through a crystal, even in the absence of an external magnetic field, seemingly contradicting conventional physical laws. These theoretical models predict a class of materials that exhibit the properties of a topological insulator. [6–10]

1.2.1 Topological Quantum Computing

To grasp the significance of these topological properties, it is crucial to examine the mechanisms that make topological insulators ideal for quantum computing applications. Notably, scientists have identified what is referred to as an "emergent" particle at the interface between two topological insulators. [11]. This particle is the Majorana fermion, a new class of matter that, unlike classical particles, serves as its own antiparticle (particles

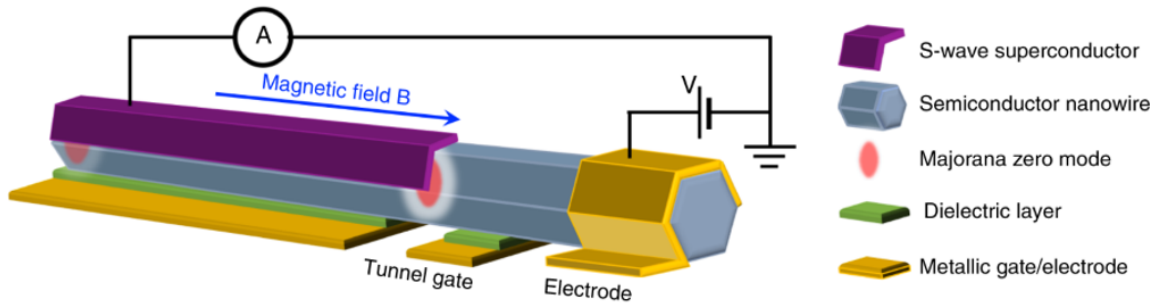

Figure 1.2: *Schematic experimental setup of the simplest Majorana nanowire device for tunneling spectroscopy measurement.* [13]

that annihilate their natural counterparts, which have the same mass but opposite electric or magnetic properties) [12]. Majorana fermions possess quantum numbers distinct from ordinary electrons. The discovery of the Majorana fermion signals promising future quantum research advancements.

Based on the principle that a particle can be its own antiparticle, Majorana Zero Modes (MZM) quasiparticles are predicted. These Majorana fermions are expected to exist in one-dimensional Fermi systems [14], marking a significant breakthrough for topological quantum computing. MZMs, bound to zero energy, follow non-Abelian statistics, and these topological states hold potential applications in Quantum Computing [15, 16]. Theoretical predictions state that MZMs have zero energy, zero charge, and zero mass. In 2012, V. Mourik and colleagues observed the first signatures of MZMs [17].

Majorana zero modes (MZMs) follow non-Abelian statistics, making them highly valuable for topological quantum computing. This concept hinges on a process known as "braiding". When the positions of a pair of MZMs are swapped, the direction of the exchange is crucially "remembered". Specifically, the result differs between clockwise and counterclockwise exchanges. The outcome of such exchanges is probabilistic, enabling the assignment of qubit states through the braiding process. Therefore, in theory, MZMs can

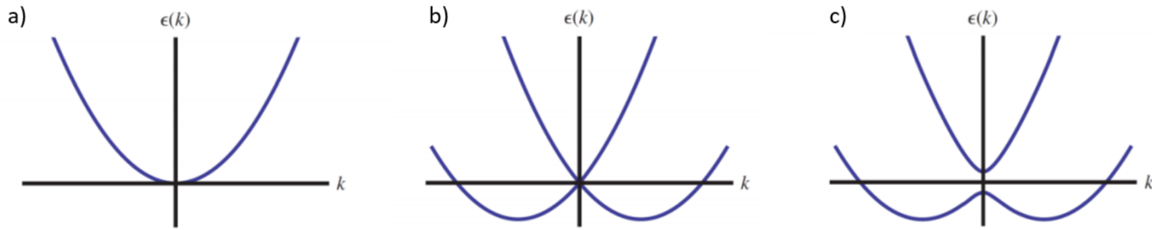

Figure 1.3: *The general evolution of the conduction band for Majorana nanowire devices. a) Single subband $E-\vec{k}$ diagram produced by gated generic nanowire. b) $E-\vec{k}$ diagram showing the effect of Spin-orbit coupling taken into account, which results in an energy shift. (c) $E-\vec{k}$ diagram displaying opening of Zeeman gap by application of a magnetic field along the axis of the nanowire.*

function as a qubit system. Due to the physical separation of MZM pairs, the information stored through braiding is protected. These non-local states render topological quantum computing exceptionally resilient to environmental perturbations.

Scientists and engineers have extensively studied this concept and platform over the past two decades. Majorana Zero Modes (MZMs) are theoretically predicted to exist in p-wave superconductors, as described by A. Yu. Kitaev in 2001 [14] and supported by other research [18]. However, p-wave superconductors do not occur naturally. In 2008, Fu and Kane suggested that an s-wave superconductor in contact with a topological insulator could produce $p_x + ip_y$ pairing [19]. In 2010, Jay Sau and colleagues predicted that coupling an s-wave superconductor with a magnetic topological insulator and a III-V semiconductor with high spin-orbit coupling could theoretically support a zero-energy Majorana fermion [20]. That same year, Lutchyn et al. proposed a simpler geometry for producing Majorana Fermions. By interfacing a 1D nanowire made of a III-V semiconductor with high spin-orbit coupling (such as InAs or InSb) and applying a magnetic field along the nanowire's long axis, MZMs should form at either end of the nanowire [21].

The theoretical requirements for creating Majorana Zero Modes (MZMs) involve sev-

eral key ingredients. Firstly, the occupation of a single subband is necessary. As illustrated in Figure 1.3(a), the energy-momentum spectrum must feature only a single occupied subband, a condition achievable by appropriately gating the semiconductor nanowire. Adjusting the gate voltage can either accumulate or deplete the wire, enabling transport through only the first subband. Secondly, utilizing a nanowire with high spin-orbit interaction causes the spin-up and spin-down components of the subband to split in momentum space, as shown in Figure 1.3(b). Thirdly, applying a magnetic field along the center axis of the nanowire can open a Zeeman gap in the energy-momentum spectrum at the $\vec{k} = 0$ point, depicted in Figure 1.3(c). At this stage, the gate voltage can be adjusted to a region in the $E - \vec{k}$ diagram where the spin and momentum of the carriers are intrinsically linked, occurring near E=0 in the schematic where the Zeeman gap has split the higher and lower energy carriers [22]. This configuration effectively mimics the band structure at the edge of a topological insulator. Lastly, by combining the particle-hole symmetry in an s-wave superconductor with the spin-polarized edge modes of the topological insulator, MZMs should theoretically form at either end of the system [19].

In this thesis, we are mainly interested in utilizing the properties of topological insulators for applications in Topological Quantum Computing. This work introduces the possibility of growth of α-Sn by using tensile strain to open up the gap as seen in Figure 1.3(c). This can be used further to proximitize with a s-wave superconductor to find the Majorana Zero Modes(MZMs).

1.3 Superconducting Quantum Computing

In 1911, H.K. Onnes first observed that the resistance of mercury vanished when it was cooled below a critical temperature, T_c [23]. This phenomenon, known as superconductivity, has been a topic of global research ever since. In his lectures on physics,

Feynman briefly explains the origin of superconductivity observed in many metals [24]. The interaction between electrons and the vibrations of the metal's atomic lattice creates a slightly effective attraction between the electrons, making it energetically favorable for them to form pairs. This pairing causes electrons, which are fermions, to behave as bosons when paired. These electron pairs, known as Cooper pairs, have the characteristic that if many pairs occupy the same energy state, almost all other pairs will do the same. Since the superconducting state of a metal occurs at very low temperatures, nearly all Cooper pairs remain in their lowest energy state. However, this electron-electron bond is quite weak and can be easily broken by a small amount of thermal energy. Hence when $T < T_c$ the electrons move in pairs and when $T > T_c$ no pairs are formed and normal electrons flow in the metal. The wave function of the Cooper-pairs in their lowest energy state can be written -

$$\psi(\mathbf{r}) = \sqrt{\rho(r)}\mathbf{e}^{\phi(\mathbf{r})} \tag{1.3}$$

where ρ is the charge density and ϕ is the quantum mechanical phase.

Superconductivity has enabled the development of fascinating physics in devices governed by the tunneling of Cooper pairs through barriers. This phenomenon allows for the creation of non-linear circuit elements, which, unlike the harmonic oscillator, have energy spectra with level splitting that varies between different energy levels. This characteristic is crucial for the realization of effective two-level systems, where the two lowest energy levels are distinctly separated from the higher states. These devices can be used to create artificial atoms at the mesoscopic scale exhibiting quantum phenomenons even though these are not of single atom size.

In their superconducting state, the Cooper pairs form a condensate on each superconductor, meaning that the electrons are in their lowest energy state and are described by

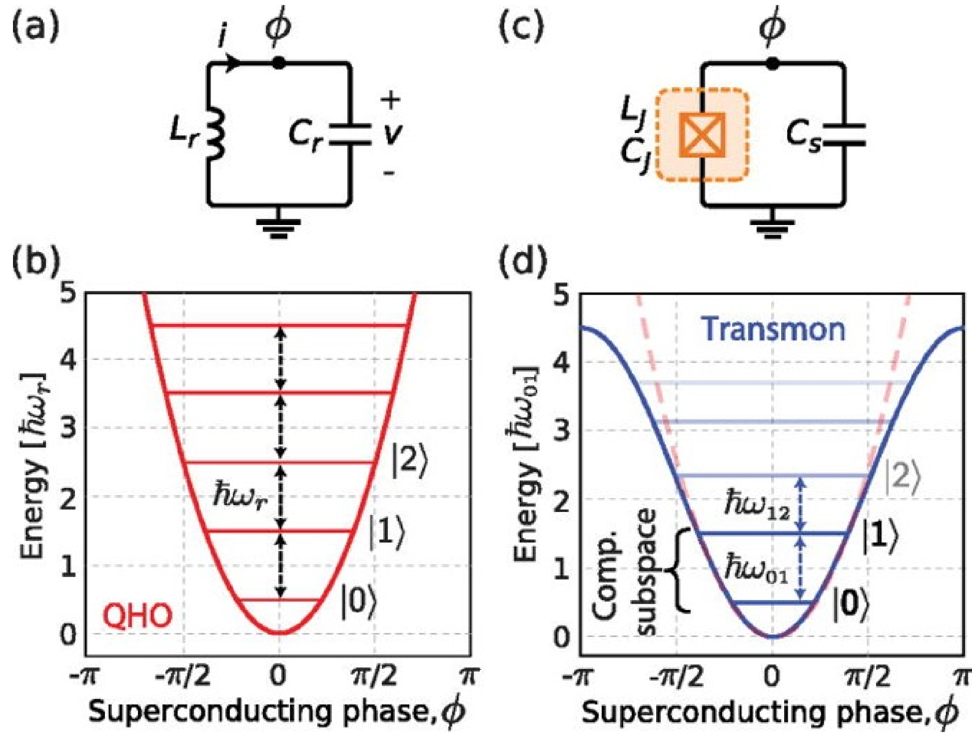

Figure 1.4: *(a) Circuit for a parallel LC-oscillator (quantum harmonic oscillator, QHO), with inductance L in parallel with capacitance, C. The superconducting phase on the island is denoted* Φ*, referencing ground as zero. (b) Energy potential for the QHO, where energy levels are equidistantly spaced r apart. (c) Josephson qubit circuit, where the nonlinear inductance* L_J *(represented with the Josephson-subcircuit in the dashed orange box) is shunted by a capacitance,* C_s*. (d) The Josephson inductance reshapes the quadratic energy potential (dashed red) into sinusoidal (solid blue), which yields non-equidistant energy levels.* [25]

the same wave function. According to the fundamental concept of quantum mechanical tunneling, if the two superconductors are separated by only a sufficiently weak link, the wave functions from both sides will overlap. i.e. interact with each other as shown in Figure 1.5(a).

To understand the dynamics of a superconducting qubit circuit, it is natural to start with the classical description of a linear LC resonant circuit as shown in Figure 1.4(a). The Hamiltonian of such an LC circuit can be thought of as a Quantum Harmonic Oscillator(QHO) -

$$H = \hbar\omega_r(a^\dagger a + \frac{1}{2}) \quad (1.4)$$

where, $a^\dagger a$ is the creation (annihilation) operator of a single excitation of the resonator.

The linear characteristics of the QHO has a natural limitation in its applications for processing quantum information. Before the system can be used as a qubit, it is important to be able to define a computational subspace consisting of only two energy states (usually the two-lowest energy eigenstates) in between which transitions can be driven without also exciting other levels in the system. To mitigate the problem of unwanted dynamics involving non-computational states, we need to add anharmonicity (or nonlinearity) into our system. Thus, to introduce the nonlinearity required to modify the harmonic potential, we use the Josephson junction – a nonlinear, dissipationless circuit element that forms the backbone in superconducting circuits [26,27]. By replacing the linear inductor of the QHO with a Josephson junction, playing the role of a nonlinear inductor, the functional form of the potential energy can be modified.

1.3.1 The Josephson effects

In 1962, Brian Josephson made a groundbreaking theoretical prediction about superconductors [26]. He determined that if two superconductors were placed close to each other, forming a weak link Figure 1.5, a zero-voltage tunneling current, known as a supercurrent, of Cooper pairs could still flow through the junction. This super-current is given as-

$$I_c = I_s sin(\phi) \quad (1.5)$$

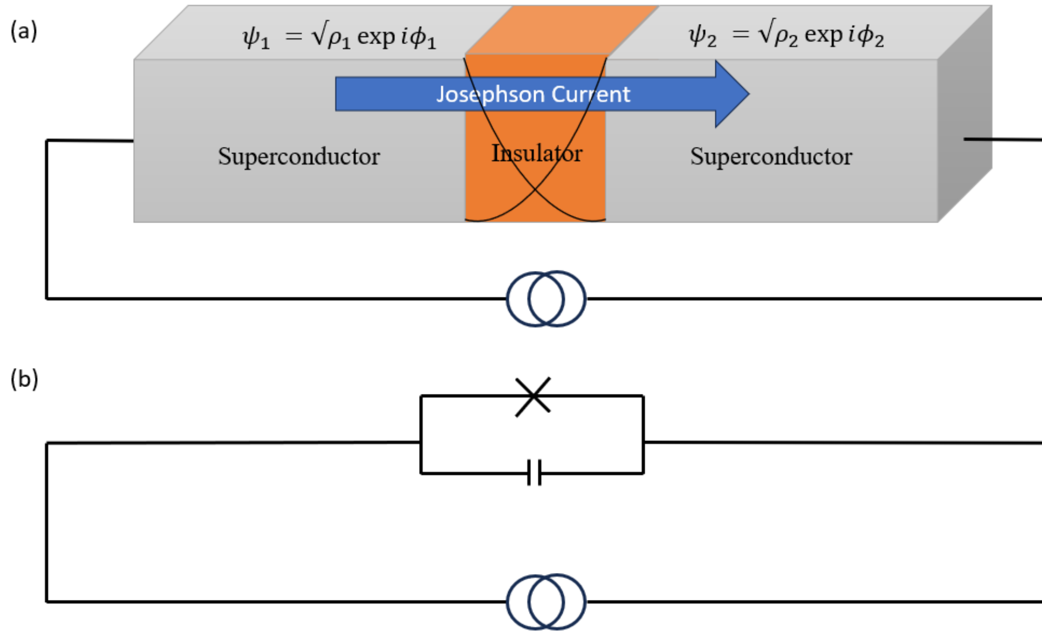

Figure 1.5: *(a)An animated Josephson junction where two superconducting electrodes are separated by a thin insulating oxide. When biasing the junction, the Cooper pairs on the two electrodes are described by the wave functions ψ_1 and ψ_2, respectively. If the oxide is made thin enough, an overlap of the wave functions gives rise to quantum mechanical tunneling of Cooper pairs. (b)The circuit diagram symbol often used for the Josephson junction.*

where $\phi = \phi_2 - \phi_1$ is the phase difference between the two superconducting electrodes and I_c is the critical current, i.e. the maximum super-current that the junction can support. The relation for the super-current in Eq.(1.5) is known as *Josephson's first relation*.

Furthermore, Josephson predicted that if a voltage was built up across the junction, the phase ϕ would evolve in time according to the following relation

$$\frac{d\phi}{dt} = \frac{2e}{\hbar} V \tag{1.6}$$

meaning that the current would now be an alternating current of amplitude I_c and

frequency $\nu = \frac{2e}{\hbar}$. Thus, the energy $E = h\nu$ equals the amount of energy required to transfer a Cooper pair across the junction. The voltage relation in Eq. (1.6) is known as *Josephson's second relation*.

Josephson junctions can be fabricated in many different ways, using many different materials. In the context of this thesis, the Josephson junctions consist of two electrodes of superconducting Tantalum grown by MBE separated by a thin insulating oxide.

1.4 Outline of the Thesis

This thesis details efforts in the Palmstrøm group to improve the current technologies used in Quantum Computing. During my Masters, I worked on materials including Superconductors and Topological Insulators. This thesis will discuss the improvements that have been made in each of those areas and the challenges faced during the course of that work.

In Chapter 2, the theory behind the growth and methods of characterizing the grown sample, and transport properties are discussed.

In Chapter 3, the *in-situ* growth of $Ta/Ta_2O_5/Ta$ Josephson Junction is shown. Fabrication of Shadow Mask is also discussed for the *in-situ* growth. Finally, the characterization of these junctions was done.

In Chapter 4, we discuss the growth of α-Sn on InSb is done. Along with that, a new method of low-temperature processing of hall bars for α-Sn has been shown. Finally, characterization and analysis of these hall bars are performed.

In Chapter 5, the contents of this thesis are summarized and future work is proposed for each of the projects presented.

Chapter 2

Growth and Characterization Techniques

2.1 The Palmstrøm Molecular Beam Epitaxy System

All the growth experiments described in this thesis were conducted using the ultrahigh vacuum (UHV) interconnected molecular beam epitaxy (MBE) system in the Chris Palmstrøm Lab. This lab features seven distinct MBE chambers, not counting several transfer chambers equipped with electron beam guns (eguns) for the deposition of caps, superconductors, and ferromagnets. Beyond the growth apparatus, the Palmstrøm MBE system boasts various tools for *in-situ* material characterization, including an X-ray photoelectron spectroscopy (XPS) setup, a variable temperature scanning tunneling microscope (VT STM), and a low-temperature scanning tunneling microscope (LT STM). These combined capabilities within a single UHV system facilitate the fabrication of complex heterostructures, such as III-Vs, ferromagnets, topological materials,

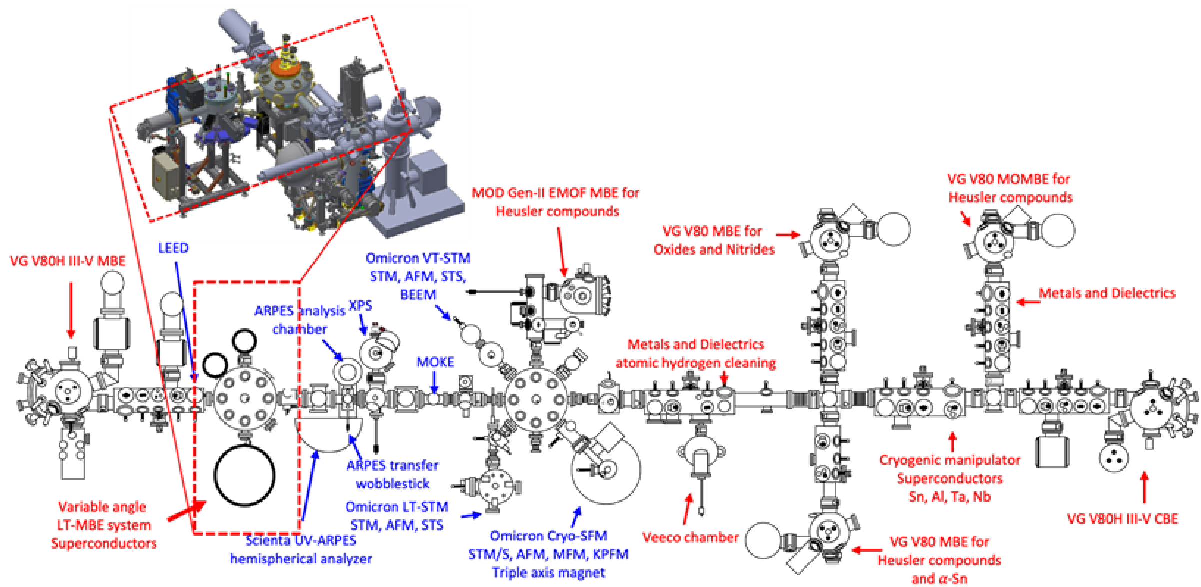

Figure 2.1: The layout of the Palmstrøm group's MBE Chamber.

and superconductors, without exposing the sample surface to contamination by breaking vacuum. Furthermore, because these growth systems are interconnected under UHV and equipped with multiple characterization tools, pristine sample surfaces can be analyzed immediately after growth, eliminating the need to remove the naturally occurring native oxide that forms in ambient conditions. The current layout for the Palmstrøm lab is depicted in Figure 2.1.

2.2 Molecular Beam Epitaxy

Molecular Beam Epitaxy (MBE) is a technique known for its precise control over crystal growth conditions. It allows the production of uniform thin films with high crystal quality and chemical purity. By layering these individual films, abrupt interfaces can be created, forming heterostructures designed for specific electronic functions. Epitaxy refers to a growth regime where single-crystal substrates are used as templates to grow single-crystal thin films.

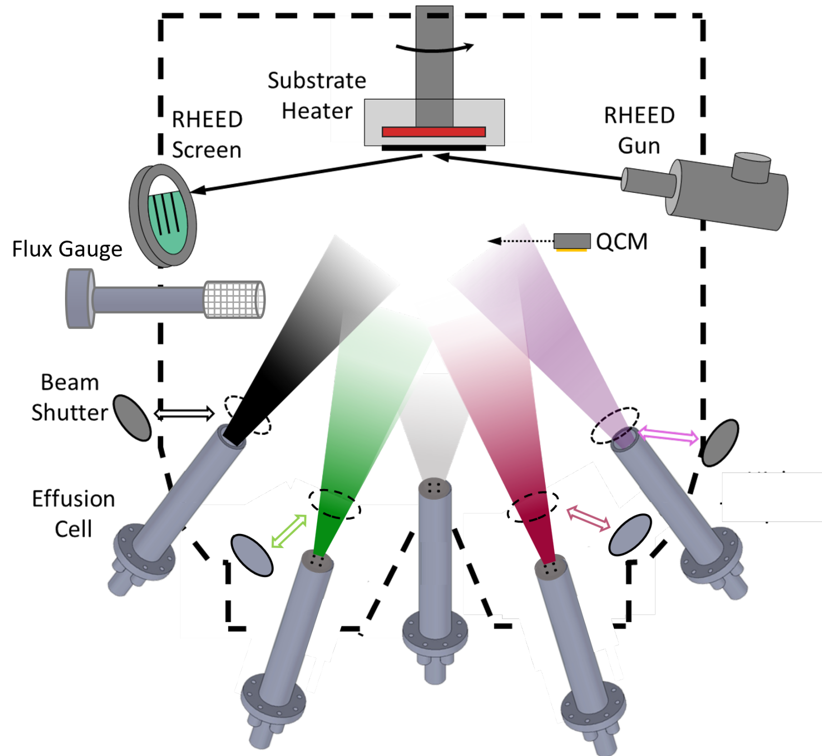

Figure 2.2: **MBE Chamber** - *Depiction of MBE chamber. Important components include effusion cells (where source material comes from), the RHEED gun (used for determining surface properties during growth), and the flux gauge (for determining flux rate).*

To achieve conditions favorable for epitaxy, MBE utilizes ultra-high vacuum (UHV) conditions, feedback-controlled substrate temperature, effusion cells with high-purity elemental sources, and low growth rates. UHV refers to pressures lower than 10^{-9} Torr, with MBE chambers often reaching base pressures in the 10^{-11} Torr range. In UHV, gas molecules have mean free paths from a few to several tens of kilometers, making them ballistic and noninteracting within the meter-long MBE chamber.

The MBE chamber is initially pumped using an oil-free roughing pump, such as a scroll or diaphragm pump, down to 10^{-3} Torr to achieve these pressures. A turbopump is then used to reduce the pressure further to 10^{-9} Torr. Ion pumps and cryo-pumps can be activated at pressures around 10^{-7} Torr, reaching very low pressures. Titanium sublima-

tion pumps can be activated at higher pressures but work effectively at lower pressures by continuously gettering reactive species. Finally, a cryo-shield filled with liquid nitrogen adsorbs residual gases like water and hydrocarbons, maintaining low temperatures to prevent outgassing and achieve the lowest possible pressures.

The substrate temperature in MBE is controlled using a proportional-integral-differential (PID) feedback controller. This controller reads the temperature from a thermocouple placed near the substrate and adjusts the current to a resistive heater to maintain the setpoint. In UHV conditions, heat transfer is primarily via infrared radiation since convection is nonexistent and thermal conduction is minimal due to the sample manipulator's geometry. As a result, the thermocouple does not measure the exact substrate temperature, often showing deviations of 50°–100°C or more, depending on the thermocouple's placement and the emissivity of the sample block and manipulator. These deviations increase with temperature.

Despite this, the substrate temperature remains consistent and stable, generally tracking with the thermocouple reading. Calibration can be improved by observing known phase transitions at specific temperatures, such as the desorption of an arsenic capping layer at 350°C. Additionally, a pyrometer can be used for substrates with well-established infrared emissivity values.

MBE (Molecular Beam Epitaxy) uses effusion cells with crucibles made of materials like pyrolytic boron nitride, beryllium oxide, or tantalum. These crucibles contain high-purity source materials, typically 4N or 5N pure, but can be as high as 7N for certain materials like Ga and As. The effusion cell heats the source material to achieve a vapor pressure in the range of 10^{-6} - 10^{-7} Torr, creating a molecular beam with an atomic flux of $10^{14} - 10^{15}$ atoms/cm^2·min. When this beam reaches the substrate, the atoms adsorb and become adatoms, which diffuse across the surface until they find the lowest energy positions, incorporating them into the epitaxial crystal. The low vapor pressure results

in a slow growth rate of $1-2$ Å/min depending on what one is growing, allowing ample time for the adatoms to integrate into the growing thin film. The growth rate can be controlled for growing different samples, e.g., GaAs can be grown at a rate of 2μm/hr or 2ML/sec.

2.3 Electron Transport Characterizations

One of the most commonly used methods of sample characterization throughout this thesis is the measurement of the electron transport properties for a variety of thin films. A Quantum Design (QD) Physical Property Measurement System (PPMS) was used for all of the transport measurements unless otherwise stated.

The Palmstrøm group's PPMS can reach temperatures as low as 1.8 K and fields as high as 14 T. Samples were prepared for the PPMS by creating Hall bars, as depicted in Figure 2.3.

Typically, vdP configuration is used for quickly characterizing sample properties as these devices can be easily fabricated by cleaving a large wafer into small, nearly square pieces. Contacts can be created using In:Sn solder and Au wires are used to connect the vdP device to a PPMS puck. The PPMS puck is subsequently loaded into the PPMS and the transport properties of the sample can be characterized. The Hall bar configuration is not as simple to make and therefore was only used to study samples of interest after screening samples in the vdP configuration. Hall bars typically require lithography followed by either wet etching or ion milling to isolate the hall bar shape. The etch or ion mill must remove enough material to at least etch the expected conduction layers into the desired hall bar shape. Otherwise, unanticipated parallel conduction may occur through the remaining material. For this thesis, a hall bar configuration was used to characterize the grown samples.

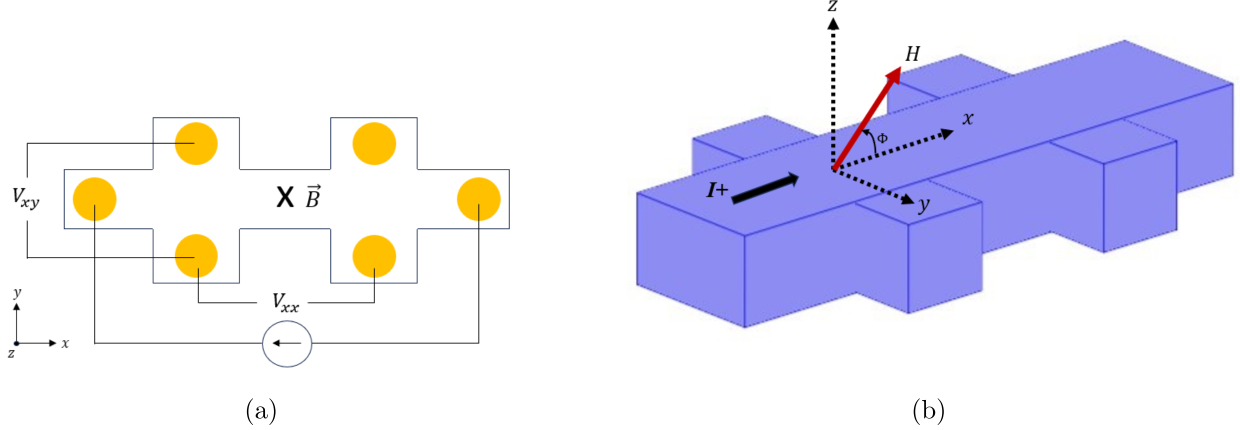

(a) (b)

Figure 2.3: **Hall Bar** - *(a) Hall bar sample configuration. Yellow areas typically correspond to areas where Ti/Au was deposited for contacts (Gates are not shown). (b) Hall bar showing how magnetic field can be rotated out of the plane.*

Hall bars as opposed to vdP measurements are much more straightforward to interpret, so we will discuss them here first. The longitudinal resistance can quickly be extracted from the sample by measuring the two longitudinally spaced pads (V_{xx}) as shown in Figure 2.3(a). By dividing the measured voltage by the applied current, I, we can determine R_{xx}. The transverse or Hall resistance can similarly be measured by measuring the transverse pads, V_{xy}, and dividing by the applied current. At $\vec{B} = 0$ we expect $V_{xy} = R_{xy} = 0$. However, as a magnetic field is applied, the Lorentz force plays a role in the electron trajectory with:

$$\vec{F} = q(\vec{E} + \vec{v} \times \vec{B}) \tag{2.1}$$

Where $\vec{F}$ is the Lorentz force, q is the charge of an electron, $\vec{E}$ is the applied electric field, $\vec{v}$ is the velocity of the electrons, and $\vec{B}$ is the applied field. Once a field has been applied and the system has reached equilibrium, F = 0, which leaves us with $\vec{E} = \vec{v} \times \vec{B}$. As the velocity of the electrons is caused by the electric field applied along the $\hat{x}$ direction

and no other direction enables current to flow in the steady state, the only nonzero component of v is v_x. Because $\vec{B}$ is only applied along the $\hat{z}$ direction, the only nonzero component is B_z. This leaves us with $E_y = v_x B_z$. By multiplying both sides of this equation by the width of the Hall Bar, w, we find:

$$V_y = V_H = v_x B_z w \tag{2.2}$$

Where V_y is the transverse voltage (also known as the Hall voltage, denoted V_H. Next, using the relationship between current and particle velocity, $J = qnv$ where n is the carrier density, we can write current as $I = qnv * A = qnv * w * t$, where t is the thickness of the conducting region. Substituting this in to Eq. 2.2, we see:

$$V_H = \frac{B_z I}{qnt} = \frac{B_z I}{qn_{2D}} \tag{2.3}$$

Where n_{2D} represents the sheet carrier density (or thickness independent) carrier density in $/\text{cm}^2$. Here we see that by applying a magnetic field, we expect to see a transverse or Hall voltage appear. This voltage is dependent upon the sign of q, and therefore on whether the dominant carriers are holes or electrons.

2.3.1 Shubnikov de Haas oscillations

In addition to observing the low-field Hall data, Shubnikov de Haas oscillations (SdH or SdHo) can be used to extract carrier density, effective mass, quantum lifetime, the Rashba coefficient, and more from magnetotransport spectra. SdH oscillations at low temperatures occur because of magnetic field-dependent fluctuations in the sample conductivity. We previously used a purely classical treatment to determine the effects of applying a magnetic field to a conductor. By treating the application of a magnetic

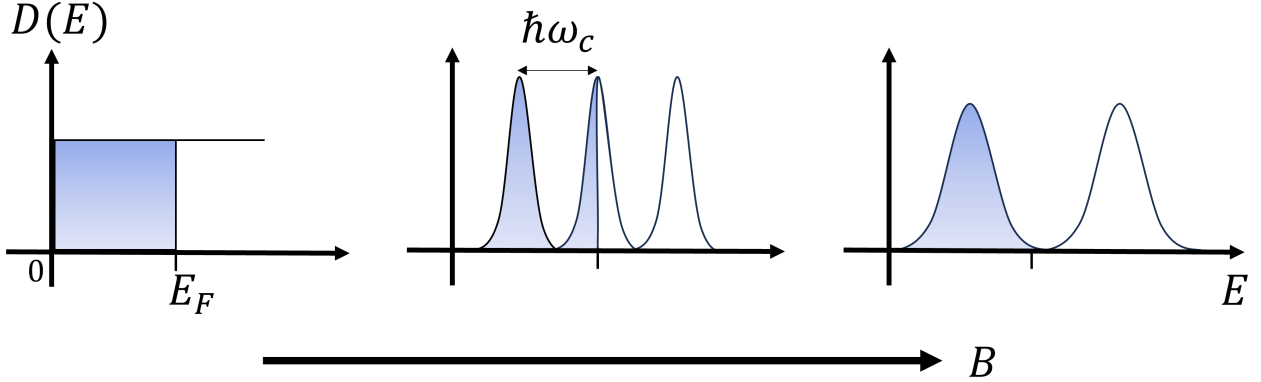

Figure 2.4: *Development of the DOS of a 2DEG in an increasing magnetic field from left to right.*

field to the conductor quantum mechanically and solving Schrodinger's equation for the energy levels of a particle in a 2DEG, the energy was found to be quantized

$$E_n = \hbar\omega_c(n + \frac{1}{2}) \tag{2.4}$$

Where n is the number of the Landau level, E_n is the energy of the Landau level, ω_c is the cyclotron frequency, and $\hbar$ is Planck's reduced constant. Using the relationship $\omega_c = \frac{qB}{m^*}$, where q is the charge of the particle, B is the applied field, and m^* is the effective mass of the particle, we can see that under an applied magnetic field, the energy of the Landau levels separate and the separation becomes larger as the applied field is increased.

A Landau Level, which energetically resides beneath the Fermi energy, is filled with N_L electrons at sufficiently low temperatures. N_L is the degeneracy of a Landau Level which is proportional to the applied magnetic field. Increasing the magnetic field entails two effects. On the one hand, the energetic separation $\hbar\omega_c$ of two LLs increases linearly with B. On the other, the degeneracy of LL (N_L) also increases linearly with B. This leads to a redistribution of electrons among the LLs to always occupy the energetically

most favorable states. For the following discussion, we will assume T = 0, so that the Fermi energy is positioned at the energetically highest occupied state and a constant charge carrier concentration.

As shown in Figure 2.4, coming from B = 0 T, the DOS transforms from a constant to a densely packed Landau-level spectrum. Further increasing B will subsequently push the LLs over E_F, as the energetic distance and degeneracy of the LLs simultaneously increase. Since the charge carrier density is constant, the number of filled states below E_F is also constant. Therefore as B increases, E_F will quickly move from an almost empty LL to the next filled LL, because the DOS on the edges of the LLs is very small compared to the center.

Therefore, whenever a LL is full and E_F sits between two LLs, one finds a minimum in the conductivity σ_{xx}. The crux of dealing with a conductivity matrix lies in its inverse, the resistivity matrix. The longitudinal element reads-

$$\rho_{xx} = \frac{\sigma_{xx}}{\sigma_{xx}^2 + \sigma_{xy}^2} \tag{2.5}$$

Surprisingly, one also finds a minimum for the resistivity. The resistance R_{xx} will oscillate as B is swept, giving rise to the Shubnikov-de Haas oscillations.

SdH are only observed in low temperatures (typically $T_{sample} < 100$ K) and reasonably high mobilities (usually $\mu > 1000 cm^2$/Vs unless high fields with $B > 10 - 20$ T are applied). This is because scattering and carrier lifetime lead to a broadening of the Landau levels. Additionally, higher temperatures lead to larger averaging of the Fermi function about the Fermi level, which weakens any potential oscillations.

Chapter 3

In-situ growth of Josephson-Junctions for Transmon Qubits

3.1 Introduction

Tantalum has been an area of interest now for applications in superconducting qubits. Recent advances in tantalum-based Transmon qubits on sapphire have demonstrated coherence times up to 0.5 milliseconds [28,29]. The growth of α-Ta at elevated temperatures is required for the realization of desirable superconducting properties. Alternatively, superconducting tantalum qubits can be grown on Si substrates by heating the substrate, but the potential formation of silicides at the Si-Ta interface could impact qubit coherence.

In this chapter, the *in-situ* growth of $Ta/Ta_2O_5/Ta$ Josephson Junctions has been demonstrated. This in-situ growth takes the help of shadow masks which help in growing structures directly on the substrate, without any need for fabrication techniques after

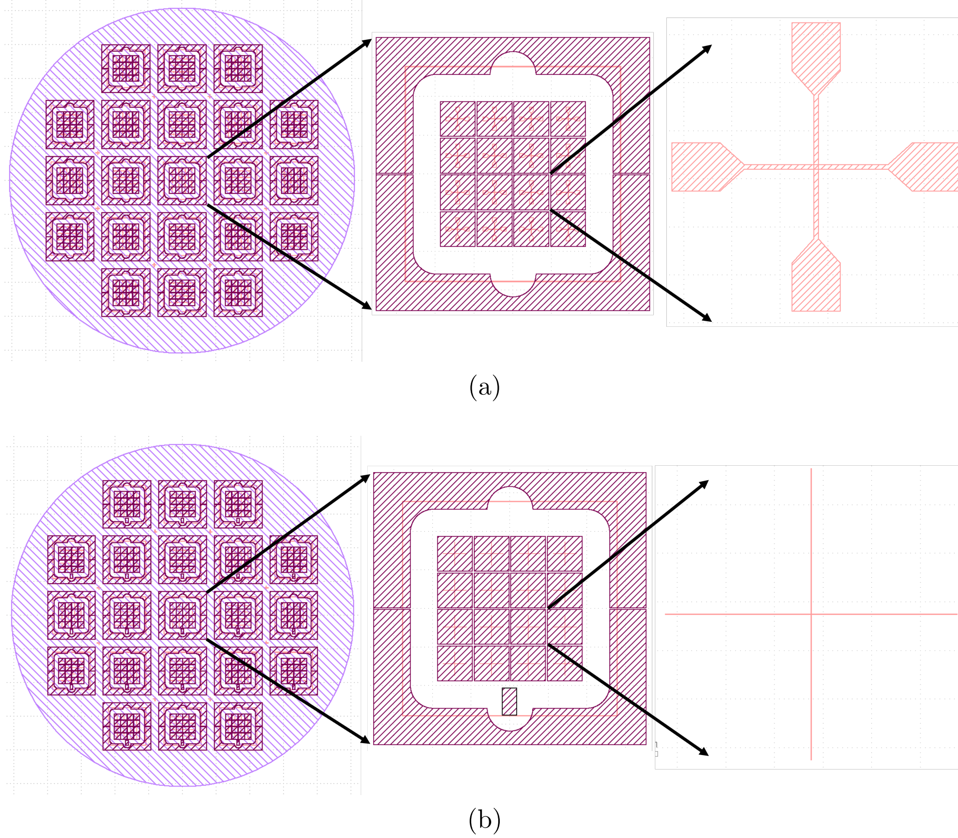

(a)

(b)

Figure 3.1: **Shadow Mask Layout** - *CAD layout of two different Shadow Mask for in-situ growth(a) Shadow Mask having electrodes of width* $20\mu m$ *(b) Shadow Mask having electrodes of width* $1\mu m$.

growth [30, 31]. This would potentially help get better surface quality and help reduce the decoherence time of the transmon qubits.

3.2 Shadow Masks Layout for in-situ growth

Two different geometries of the Josephson Junctions were designed as shown in Figure 3.1. In total 21 shadow masks were designed for fabrication in a 4-inch Silicon Wafer. For the growth of the Josephson Junctions, two different shadow masks are needed - one for the horizontal electrode and one for the vertical. So, out of 21 shadow masks, 20 of them can be used for the growth of Josephson Junctions.

The first design is made as shown in Figure 3.1(a). The leads were 20μm in thickness each which gave an area of the junction to be 400μm^2. This structure was designed to see if the junction to be fabricated would superconduct as it does for thin films of Tantalum. The second design as shown in Figure 3.1(b) has leads of width 1μm with each having an area of 1μm^2. The second design theoretically should have a lower T_c and be more practical than the first design.

As the area of a Josephson Junction increases, the critical temperature (T_c) can change due to several intertwined factors. Larger junctions often face challenges in maintaining uniformity in material properties, such as thickness and composition, which can introduce local variations affecting the overall T_c. Thermal properties also play a role, as larger junctions may experience different heat dissipation and thermal gradients, leading to non-uniform temperature distributions that influence the measured T_c. Moreover, susceptibility to magnetic flux penetration increases with size, potentially disrupting the superconducting state and altering T_c. The distribution of Josephson current density might change with area, impacting the junction's superconducting behavior. Additionally, the relative influence of edge effects can vary with size, affecting the overall superconducting properties.

3.3 Fabrication Methodologies

3.3.1 Si Wafer

The fabrication of the shadow masks started with using a Si(001) wafer with 200nm of SiN_x grown on both sides using Low-Pressure Chemical Vapor Deposition. The use of this wafer with the SiN_x membrane is of utmost importance which is seen in the next sections.

The fabrication of the Shadow Mask is done by processing both the Front and the backside of the Si wafer. First, the Topside processing of the patterns for the Josephson junction is defined and then the back side of the wafer is aligned with the top side to etch down the silicon wafer from the back and open up the membrane eventually. The fabrication of the top and back sides to form the shadow masks is as follows.

In this section, the fabrication methods and tools which are used are described.

3.3.2 Process flow for the Shadow Masks

The procedure commences with a Si wafer that has been coated with 200 nm of SiN_x, applied through LPCVD. This wafer is subsequently prepared for surface patterning to facilitate the formation of openings for the Josephson Junctions. Electrodes for these junctions were fabricated in two widths: 20μm and 1μm. The wafers post-lithography are illustrated in Figure 3.2. AZ4110 was utilized as the photoresist, with lithography conducted at a dose of 200μC/cm^2, a parameter crucial for pattern quality. To develop the resist, the sample was submerged in an AZ400K 1:4 solution for 75 seconds.

Following patterning, the wafer underwent etching of the silicon using Fluorine ICP etching, specifically employing a CF_4/O_2 gas mixture for a duration of 4 minutes. During this phase, the SiN_x layer, previously grown via LPCVD, exhibited an etch rate of approximately 60 nm/min.

Subsequently, the wafer was transferred to a PECVD system to deposit a 100 nm layer of low-stress SiN_x, intended to safeguard the etched patterns on the underlying LPCVD-grown SiN_x layer. After deposition, the top surface was coated with photoresist and subjected to a baking process to further preserve the etched designs.

Next, comes the backside alignment of the wafer. For that, the backside was coated with AZ4110 photoresist. Alignment marks were patterned on the back using a contact

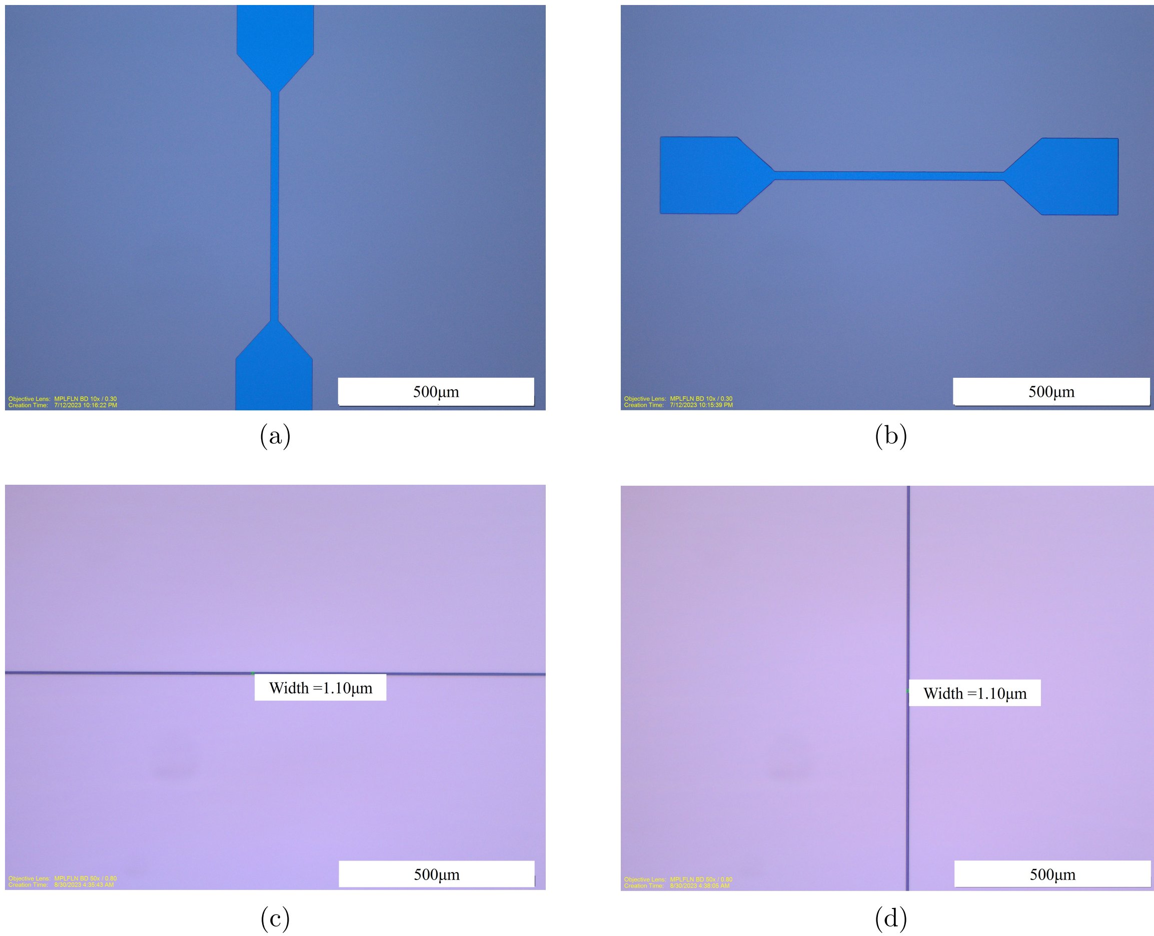

Figure 3.2: **The patterns of Josephson Junction after Photolithography** *(a-b) The patterns show the electrodes with a width of* $20\mu m$ *(b-d)The patterns show the electrodes with a width of* $20\mu m$.

aligner (SUSS MA-6) which were aligned with the patterns on the top side. Then, these alignment marks were used to align the top side and the back side of the wafer. The patterns for the backside were then exposed by a Maskless Aligner (Heidelberg MLA150). Patterns were developed using AZ400K 1:4 solution and were ready for etching. The patterns with the SiN_x were then etched using CF_4/O_2 etch for 12 mins. The photoresist was then cleaned off using Acetone, Isopropyl (IPA) and Deionized water. Finally, the wafer was dipped in KOH solution heated at 87°C to etch the silicon from the back. After 8 hours of etching with KOH, the wafer was taken out of the solution.

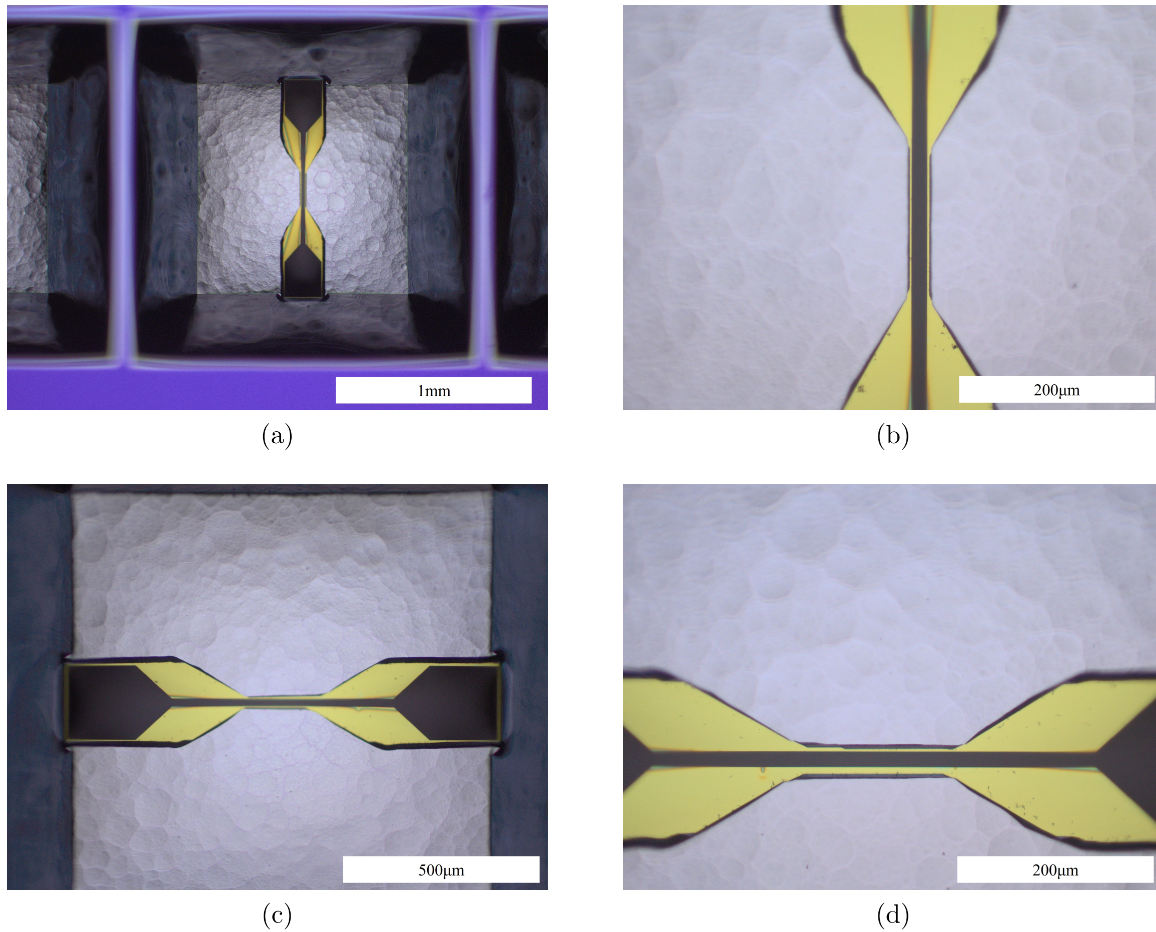

Figure 3.3: **KOH Etch** - *Backside of the Silicon Wafer after KOH Etching opening up the patterns for the first design in the* SiN_x *layer in the front.*

Buffered HF was then used to etch down the PECVD-grown SiN_x for 210 seconds. Buffered HF is very sensitive to hydrogen content. LPCVD and PECVD grown SiN_x having different hydrogen content [32, 33] helps the HF to selectively etch PECVD grown SiN_x.

The wafer was then put again in the heated KOH solution for the final etching of the silicon till the SiN_x patterned membrane started to show up. This is shown for both shadow masks in Figure 3.3 and Figure 3.4(a). The final wafer after the processing is shown in Figure 3.4(b)

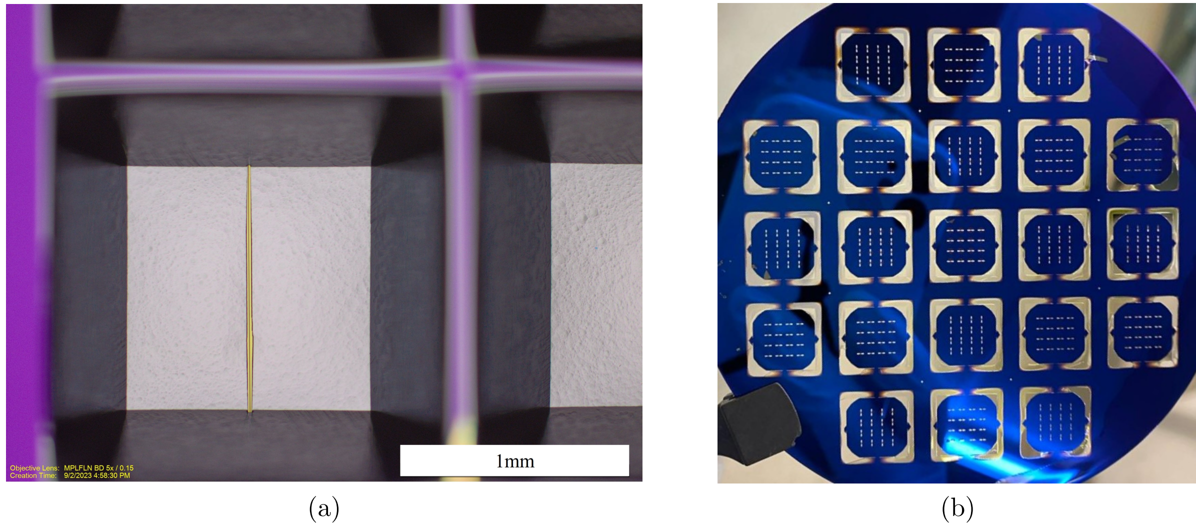

(a) (b)

Figure 3.4: **KOH Etch** - *Backside of the Silicon Wafer after KOH Etching opening up the patterns for the second design in the SiN_x layer in the front.*

The wafer is then cleaned using Acetone and IPA and cleaved to grow the JJs in the MBE system. The whole recipe for making the shadow mask is shown in Appendix A.

3.4 Growth of the Ta/Ta_2O_5/Ta Josephson Junctions.

3.4.1 Low-Temperature Molecular Beam Epitaxy (LT MBE)

For the growth of the JJs, Low-Temperature Molecular Beam Epitaxy(LT-MBE) was used. The unique cryogenic low-temperature Molecular Beam Epitaxy (LTMBE) system in the Palmstrøm laboratory at the University of California Santa Barbara is connected to other MBE systems, *in-situ* characterization equipment, and preparation chambers allows both careful preparation and studies of the substrate surface before cryogenic film growth but also at different stages of the growth without surface contamination. The LTMBE allows the deposition at substrate manipulator temperatures down to $\sim$5K, which results in an estimated sample temperature $<$20K, integrates them into various

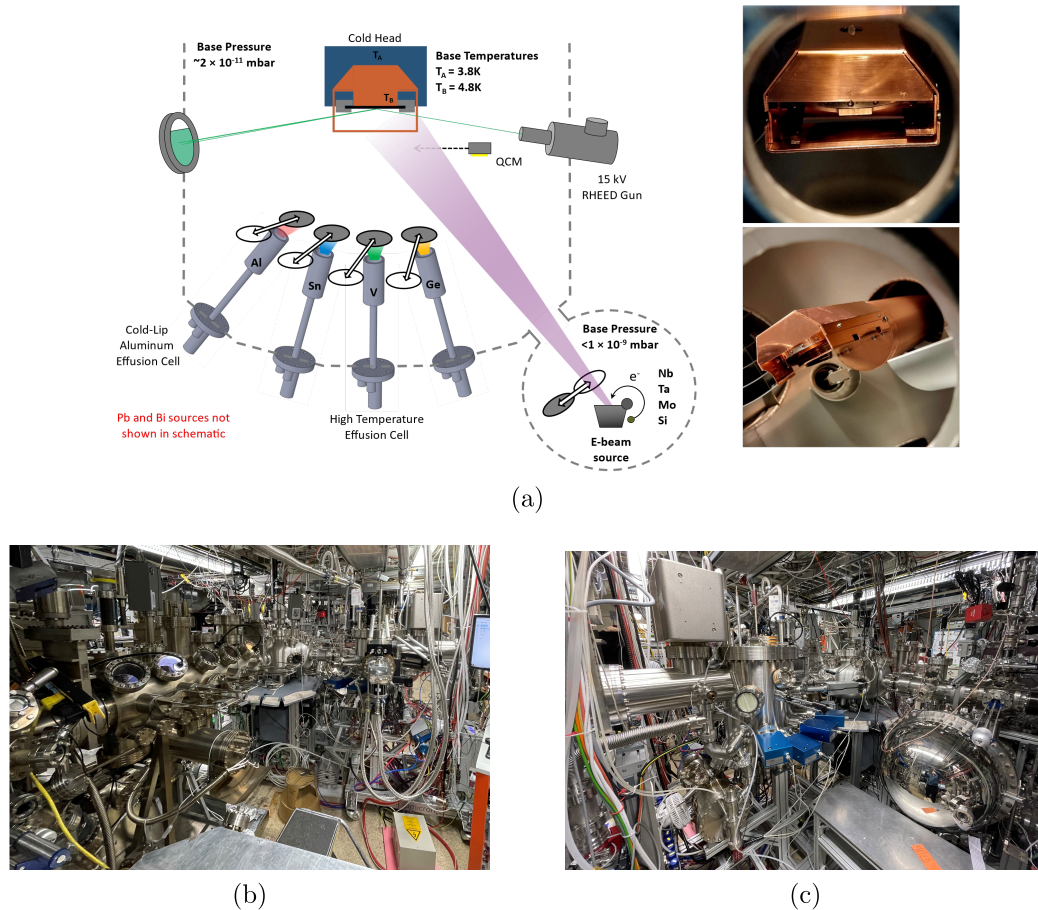

(a)

(b) (c)

Figure 3.5: **Schematic of the LT MBE** - *(a) Depiction of MBE chamber. Important components include effusion cells (where source material comes from), the RHEED gun (used for determining surface properties during growth), and the cold head.(b-c)LT EVO 50 MBE in the Palmstrøm Lab.*

systems and structures, and analyzes them using a multitude of surface science tools (STM/STS, AFM, XPS, Auger, ARPES) without exposing them to air. Currently, the LTMBE system has thermal effusion cells loaded with Al, V, Pb, Sn, Bi, and Ge, along with a 4-pocket electron beam source containing Si, Nb, Ta, and Mo. This is shown in Figure 3.5.

Reflection high-energy electron diffraction (RHEED) is used for *in-situ* characterization during growth and subsequent warming in the LTMBE system.

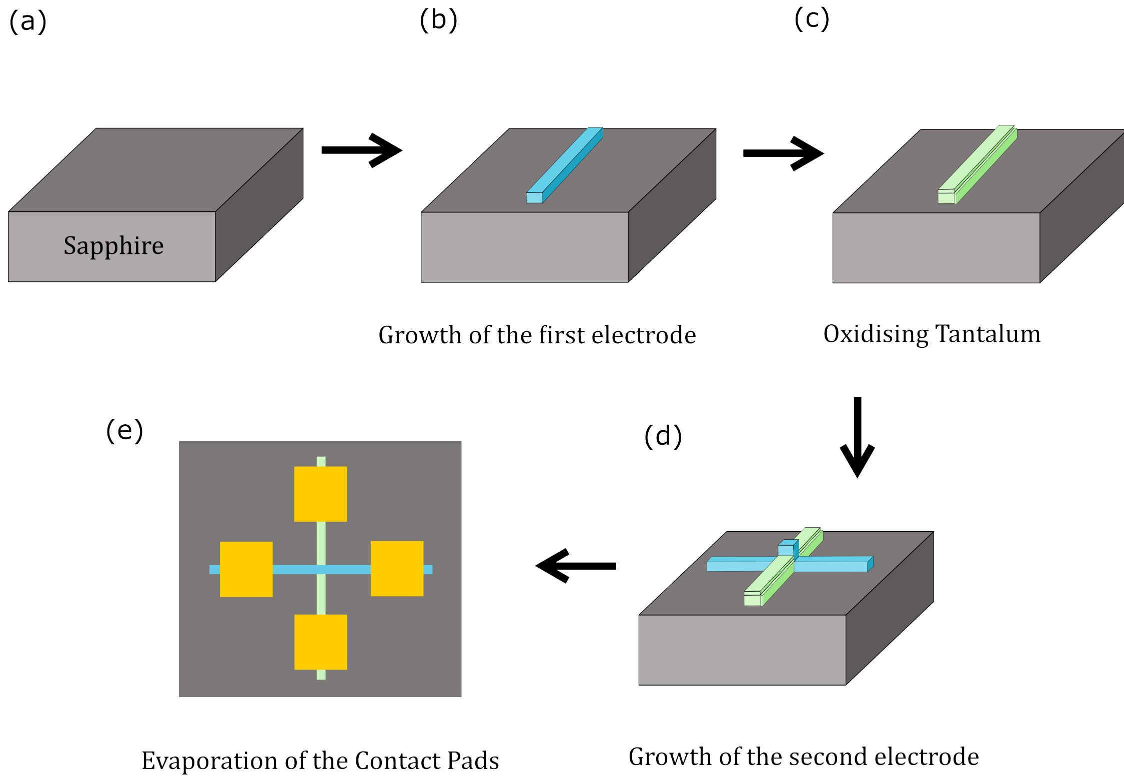

Figure 3.6: *Growth Process for the Ta/Ta_2O_5/Ta Josephson Junction. The blue color shows Tantalum electrodes, and the green shows Ta_2O_5.*

3.4.2 Sample preparation

The substrates used in this report are 3" diameter Al_2O_3(0001). These samples were coated in resist and diced into 10 x 10 mm samples. The substrates were cleaned with solvents and etched in a 3:1 H_2SO_4:H_2O_2 piranha solution for 5 minutes. Then, the substrates were loaded into the ultrahigh vacuum system followed by a degas and anneal at a thermocouple temperature of 700°C. Figure 3.6 shows, the schematic of the growth of the Josephson Junction and the fabrication of the contact pads.

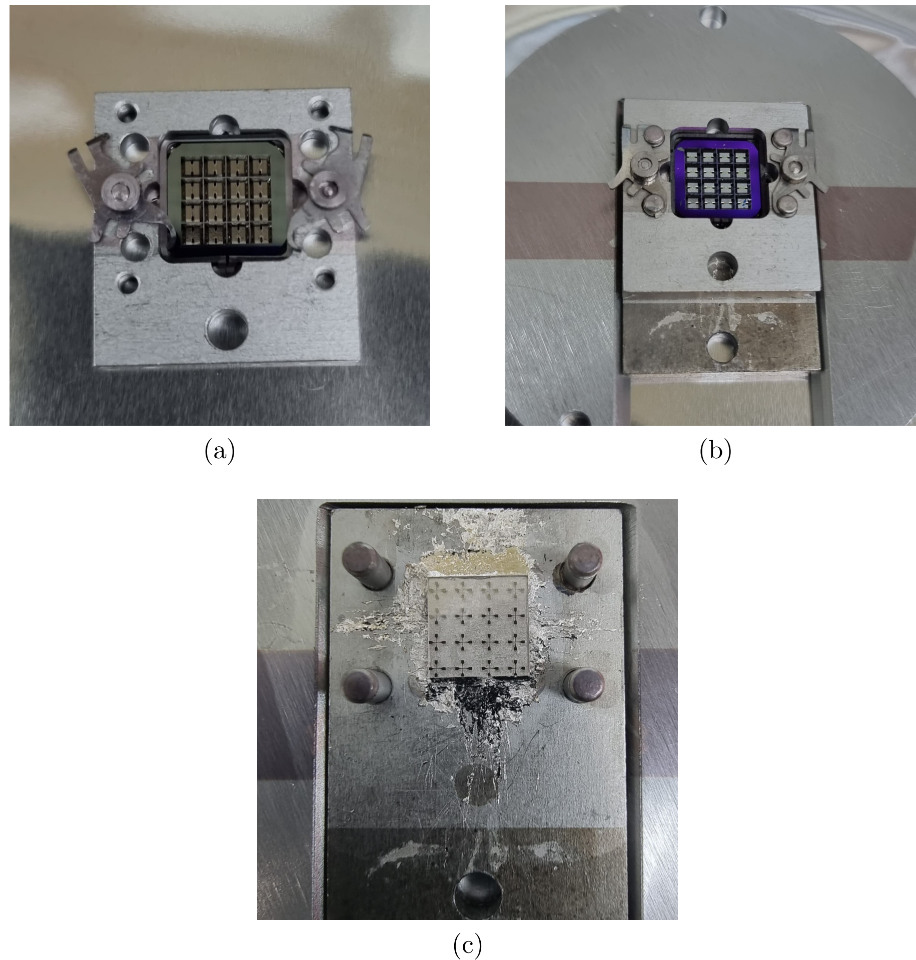

(a) (b) (c)

Figure 3.7: **Trasnfer of Shadow Mask***(a)Shadow mask being fitted in the block (b) The shadow mask being slid into proximity to the sample for growth (c) Sample after the growth.*

3.4.3 Transfer of Shadow Mask

The precise positioning of the shadow mask proximal to the sample is crucial for the growth process. Each shadow mask is cleaved from the wafer as illustrated in Figure 3.4(b) and subsequently affixed to a block using clips, as depicted in Figure 3.7(a). These clips, visible on the side of the block, are rotated to secure the shadow mask in place.

On a separate block, the sample is bonded using indium. This block features four pillars designed to facilitate the alignment of the shadow mask with the sample. This

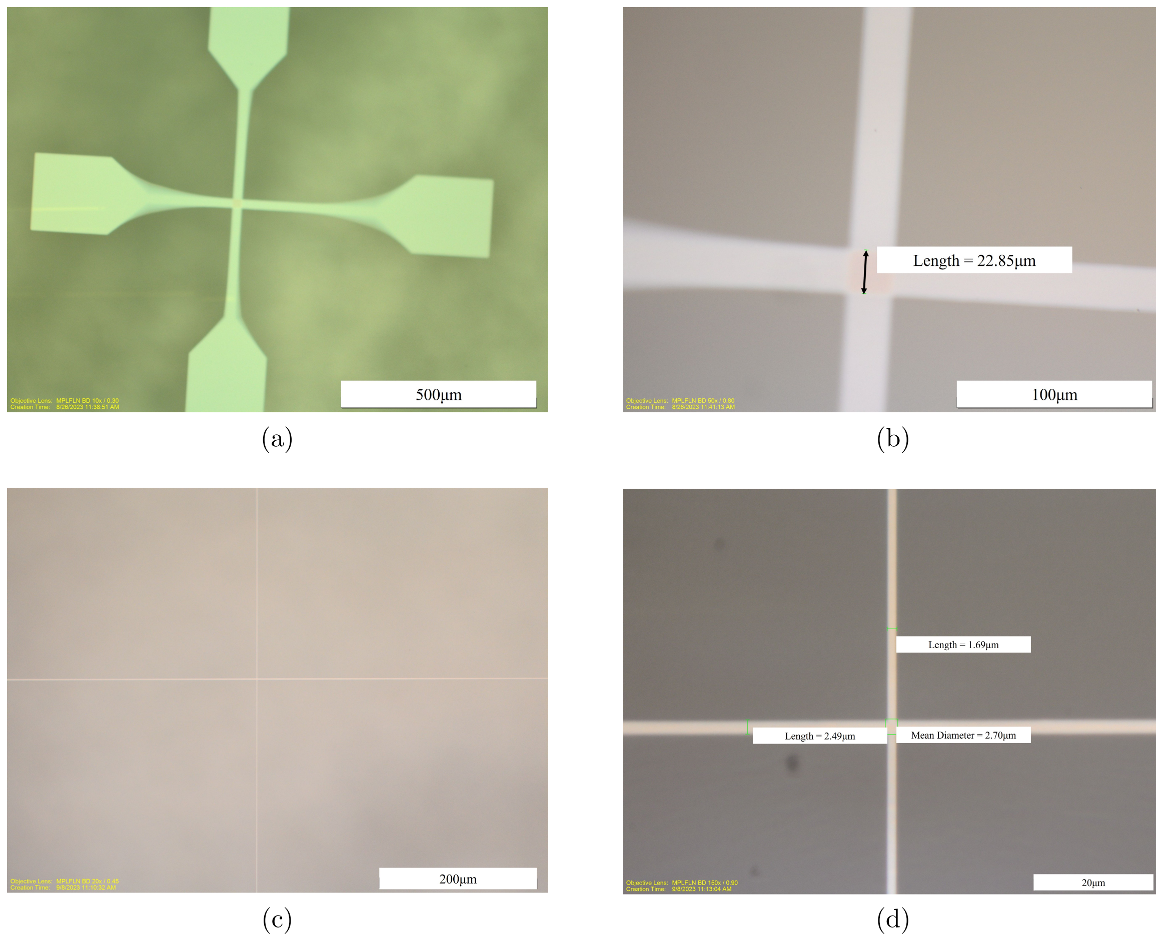

(a) (b) (c) (d)

Figure 3.8: **After Growth***(a-b) 400μm^2 Ta/Ta_2O_5/Ta Josephson Junction (c-d) 1μm^2 $\times$1μm Ta/Ta_2O_5/Ta Josephson Junction.*

alignment process is visually detailed in Figure 3.7(b), showing the shadow mask being slid over the pillars to a position near the sample. Following alignment, this assembly is transferred into the MBE chamber for the deposition process.

After the growth cycle, the block is removed from the system, and the sample is extracted. Figure 3.7(c) captures the post-growth state of the sample and highlights the pillars used to guide the block carrying the shadow mask.

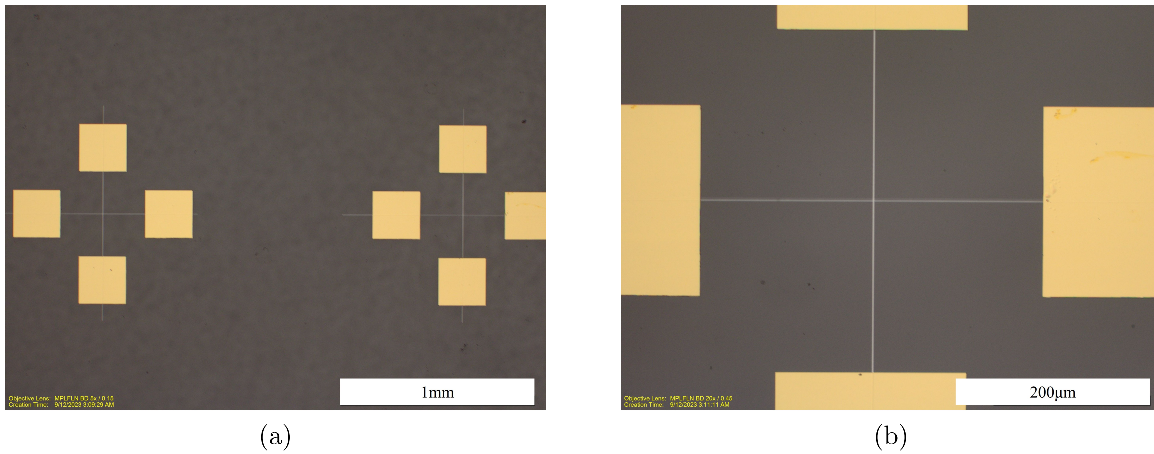

(a) (b)

Figure 3.9: **Contact Pads**-*Final Device after fabrication of the Ti/Au contact pads.*

3.4.4 Growth of Josephson Junctions

The growth was done in Scienta Omicron LT EVO 50 MBE chamber with an LN_2 shroud holding a base pressure of 2 x 10^{-11} mbar. Tantalum was evaporated from an electron beam evaporation source in an additional chamber separated by a gate valve. Ultra-high vacuum conditions remain during Ta deposition, with the main chamber pressure staying below 1×10^{-10} mbar. The cryogenic manipulator allows for temperatures ranging from 300K down to 6K during growth. The temperature is measured near the substrate with a Si diode. The actual substrate temperature is believed to be less than 10 K warmer as determined by attaching a thermocouple on a dummy block with the radiation from the cell at 1000 °C impinging on the dummy block. Growth rate and thickness were monitored using a Quartz-Crystal-Microbalance.

First, a shadow mask was transferred with the sample mounted on a block as described in section 3.4.3. The growth was conducted for Ta growing a film of 15nm on the bottom. The dielectric layer was formed with Ta being exposed to oxygen. Finally, another shadow mask was mounted with the sample and then growth was performed forming the cross pattern as seen in Figure 3.8. Thus, the Ta/Ta_2O_5 Josephson Junction was formed. The

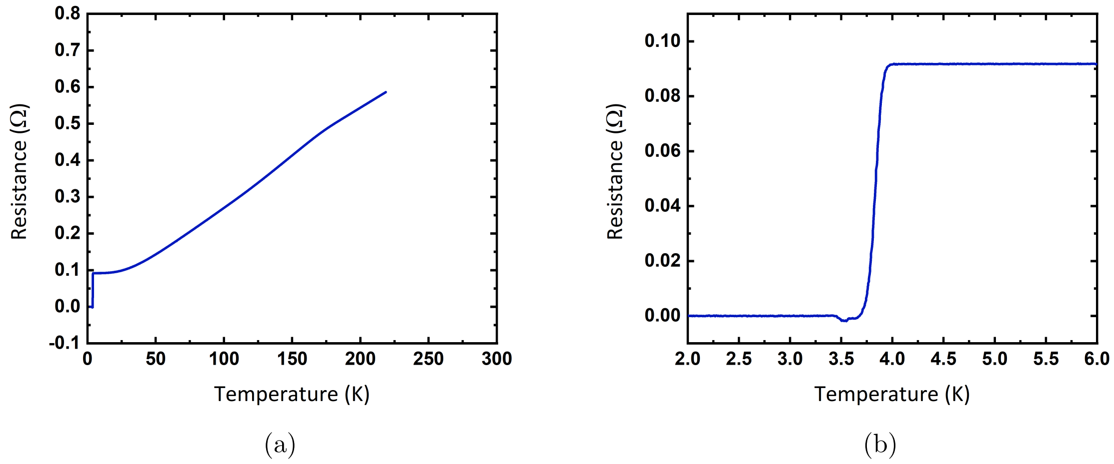

Figure 3.10: **Electrical Characterization-** *(a) Resistance vs. Temperature from 300K to 2K (b) Superconducting transition at 4K.*

growth was performed with the collaboration of my group member Teun Van Schijndel.

To measure the transport of this device, contact pads were needed where it could be probed. The contact pads were patterned by direct lithography and then Ti/Au contacts were deposited via $ex-situ$ electron beam evaporation. The final device is shown in Figure 3.9.

3.5 Results and Discussion

In this section, the transport properties of both devices were characterized using the Quantum Design Physical Property Measurement system. Both the devices were cooled down to 2K from room temperature. DC measurements were performed sweeping the current from -15mA to 15mA.

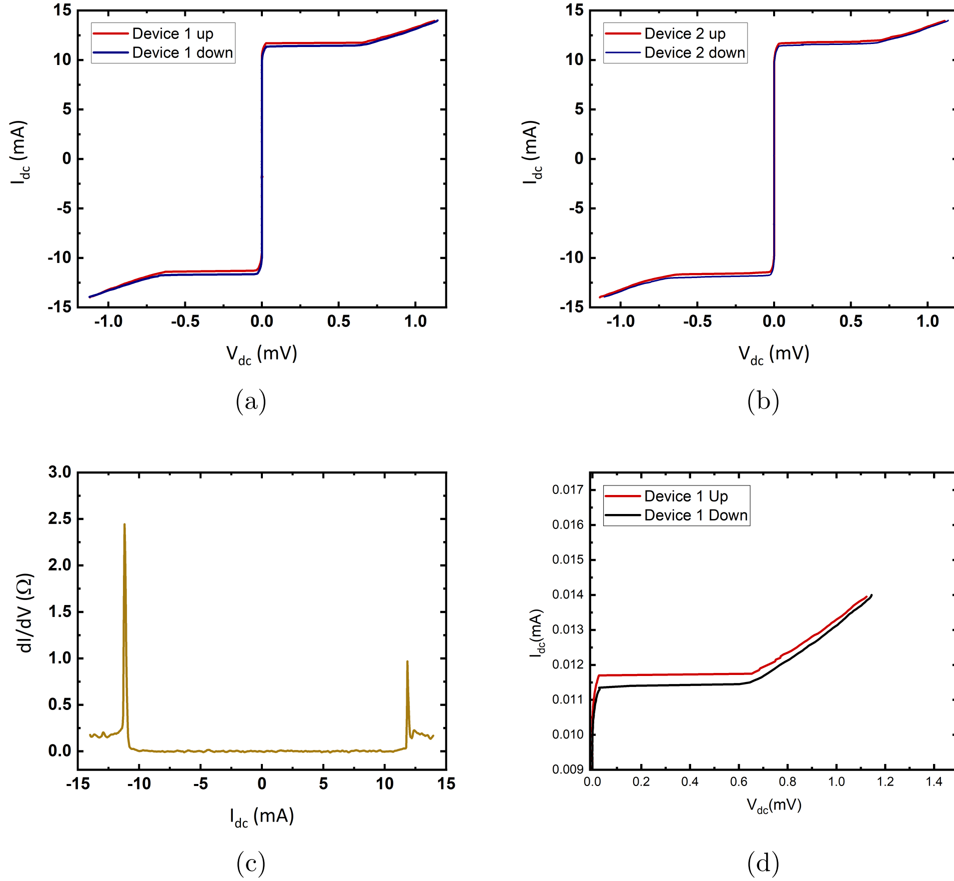

Figure 3.11: **Electrical Characterization** - *(a-b) Current vs. the Voltage of two devices on the same chip with a current sweep from -15mA to 15mA. (c) The slope of the IV characteristics vs. bias current showing peaks for the inverse of resistances (d) Current vs. voltage of the Josephson Junction showing hysteresis .*

3.5.1 400μm^2 Ta/Ta$_2$O$_5$/Ta Josephson Junction

For each sample grown, 16 devices can be measured of which 2 samples were measured. First, the temperature dependence of the device is seen in Figure 4.15. Figure 4.15(a-b) shows the change in resistance as the sample is cooled down. This drop in resistance is essentially due to the junction was seen indicating the critical temperature of the film with T$_c$ of 4.0K. Similar characteristics are seen in the resistance transition as reported before [34]. The Residual Resistance Ratio (RRR) of this device was calculated to be 9.2.

Residual-resistivity ratio is usually defined as the ratio of the resistivity of a material at room temperature(300K) and at 0 K. Of course, 0 K can never be reached in practice so for this case we calculate RRR as-

$$RRR = \frac{R_{300K}}{R_{10K}} \tag{3.1}$$

Next, both the devices were measured by sweeping the DC current from -15mA to +15mA. As seen from Figure 3.11(a,b) the critical current(I_c) of the system is found 11.8mA. The resistance of the circuit can be found from the slope in Figure 3.11 which denotes a 1/R relation. This slope is found by taking the derivative of the current wrt. voltage (dI/dV). This is shown in Figure 3.11(c). The resistance of the device when the current is increased beyond I_c is 4.16Ω. In Figure 3.11(d), a zoomed-in portion of the current vs voltage curve is shown. This is shown to show there is hysteresis in the I-V curve of the sample because of heating by the current through resistive filters on the sample stage.

3.5.2 1μm^2 Ta/Ta_2O_5/Ta Josephson Junction

For the second JJ with an area of 1μm^2, there was no superconducting transition seen at 4K. The resistance vs. temperature is shown in Figure 3.12(a) as the sample was cooled down from room temperature. A decrease in resistance has been seen though a superconducting transition was not seen at a temperature of 2K. It can be anticipated that if the sample is cooled down more to 50mK, a superconducting transition might be seen, though this statement requires more experimental evidence.

During the growth of the second electrode, there is an additional thin layer of Tantalum which is evaporated which can be due to the shift of the shadow mask during the growth process as seen in Figure 3.12(b).

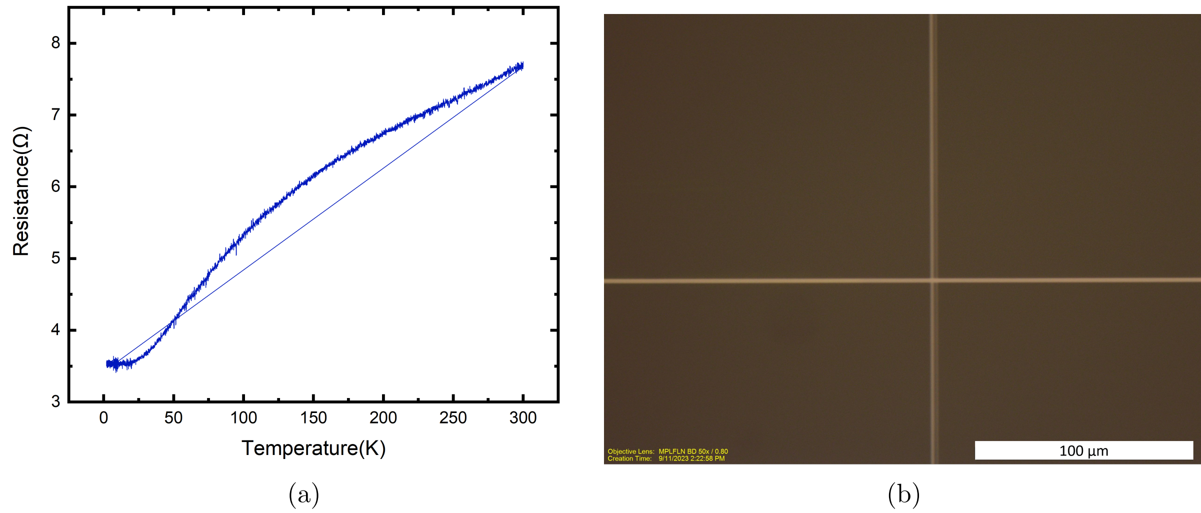

(a) (b)

Figure 3.12: **Electrical Characterization-** *(a) Resistance vs. temperature from 300K to 2K (b) A problem which occurred during growth due to shift in shadow mask.*

3.6 Conclusion

In conclusion, *in-situ* growth of Josephson Junction has been demonstrated by the use of Shadow Masks. The fabrication of shadow masks has been fully discussed. Low-temperature growth of Tantalum shows promising advancements for realizing superconducting qubits. The Josephson junction growth paves the way for such qubits which can potentially have a higher decoherence time. The 400μm^2 junction showed a superconducting transition at a temperature of 4.0K with an RRR of 9.2. Along with that, the junction had a critical current(I_c) of 11.8mA. Though the second device didn't have a superconducting transition, it can be a region of interest for future work.

Chapter 4

α-Sn for Topological Quantum Computing.

4.1 Introduction

Alpha tin (α-Sn), also known as gray tin, is a material of great interest due to its unique electronic properties and its potential as a topological insulator. Topological insulators are materials that conduct electricity on their surface while remaining insulating in their bulk. These surface states are protected by time-reversal symmetry and are robust against perturbations, making them promising candidates for applications in spintronics and quantum computing.

Alpha tin crystallizes in the diamond structure, similar to silicon and germanium, but exhibits distinct electronic properties. Bulk crystal of tin has two main crystalline forms, gray(α) and white(β) tin, which exhibit body-centered tetragonal A4 and face-centered cubic (fcc) A5 structure respectively as shown in Figure 4.1. The α-Sn and β-Sn crystallize in a diamond structure and tetragonal symmetry respectively. The allotropic configurations of tin can be transformed into one other at 286.2K. The β-Sn behaves

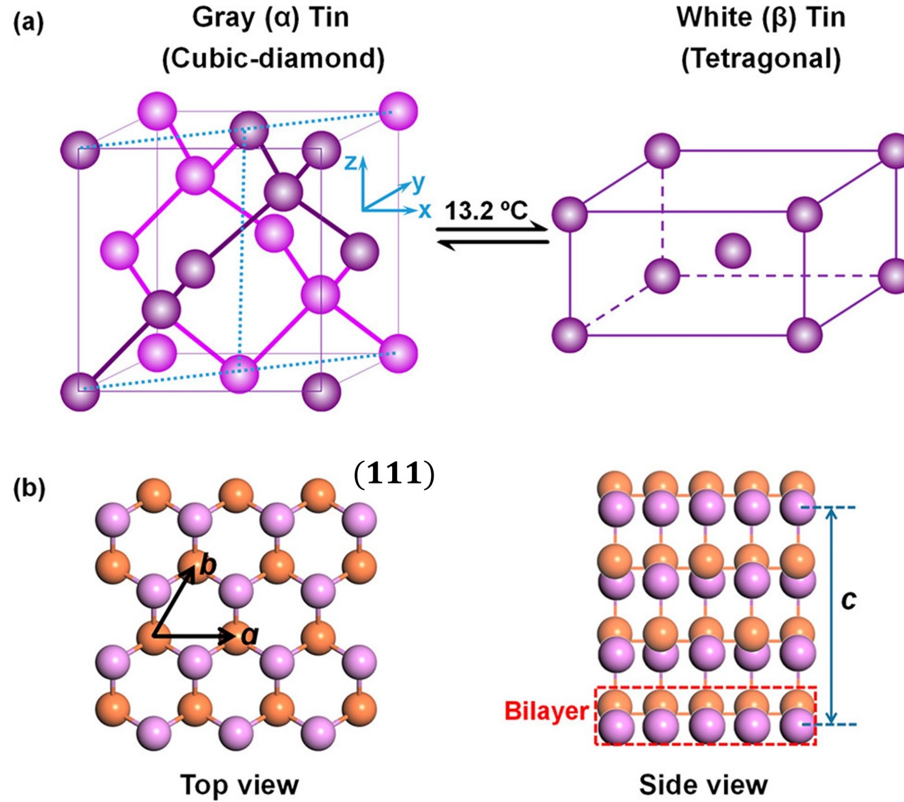

Figure 4.1: *(a) Ball and stick models of the gray α-tin and white β-tin. (b) (left) Top and (right) side views of the (111)-orientated crystal structure of α-tin film, $a = b = 4.58$ Å, $c = 11.24$ Å. The purple and orange balls in panel b represent tin atoms at different heights. The red dashed rectangle in the side view shows the bilayer unit of α-Tin.* [36]

as a superconductor below 3.72K, where the Meissner effect was first discovered [35]. However, epitaxially grown thin films of tin tend to form a α-phase. Figure 4.1(b) shows the (111)-oriented α-Sn film, which exhibits a graphene-like honeycomb structure but is buckled with the atoms in sublattices at different heights in AA stacking mode.

The band structure of α-Sn is characterized by an inverted band ordering at the Γ-point in the Brillouin zone [37], which is essential for the realization of a topological insulator. This inverted band structure leads to the formation of topologically protected surface states when α-Sn is subjected to appropriate conditions, such as strain. Strained α-Sn, particularly when grown on substrates like InSb(001), can exhibit a topological

insulator phase [38]. The strain induces a slight modification in the lattice parameters, affecting the electronic band structure, opening a small band gap at the Γ point, and facilitating the formation of topological surface states. These states are characterized by spin-polarized edge channels that are protected from backscattering, enabling dissipationless transport.

The molecular beam epitaxy (MBE) system is an ideal technique for the epitaxial growth of high-quality α-Sn films on InSb(001) substrates. MBE allows for precise control over the deposition process, enabling the formation of atomically smooth and uniform films with minimal defects. The choice of InSb(001) as a substrate is particularly advantageous due to its lattice match with α-Sn, which helps minimize strain-induced dislocations and defects. Experiments have suggested that on InSb, α-Sn thin films go through multiple topological phase transitions between two-dimensional (2D) Topological Insulator(TI), three-dimensional (3D) TI, 2D Dirac semi-metal(DSM), 3D DSM, and normal insulator as a function of surface orientation, strain, and film thickness, generating much interest as a testbed for topological phase transitions [39–44].

Extensive studies on bulk single crystals of α -Sn have demonstrated controlled dopant concentration and confirmed its inverted band structure. For thin-film growth, InSb is the primary substrate chosen for surface science investigations of α-Sn. This growth process typically involves molecular-beam epitaxy (MBE) on sputter-anneal cleaned InSb, resulting in an indium-rich surface. Indium, known to act as a p-type dopant in bulk α-Sn [45], readily incorporates into α-Sn thin films from the InSb substrate [46, 47].

The study of α-Sn as a topological insulator and its epitaxial growth on InSb(001) substrates in an MBE system represents a significant advancement in the field of condensed matter physics. The unique electronic properties of α-Sn, combined with the precise control offered by MBE, make it an excellent candidate for exploring new quantum phenomena and developing advanced electronic and spintronic devices. This chapter

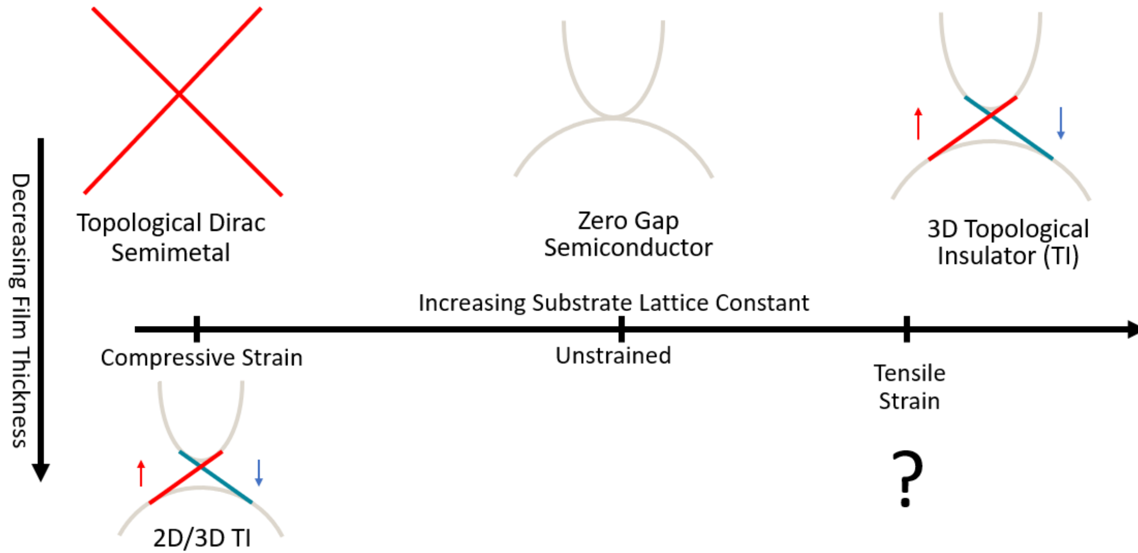

Figure 4.2: *Flow chart showing different phases of α-Sn when unstrained, grown with compressive or tensile strain as a function of film thickness.*

provides a detailed overview of the fundamental properties of α-Sn, the epitaxial growth process, and the realization of the topological insulator phase, setting the stage for further research and applications in this exciting field.

4.2 Growth of α-$Sn_{1-x}Ge_x$ on InSb

4.2.1 Motivation

Unstrained α-Sn has a diamond structure at 13.2°C as shown in Figure 4.1. As seen from the literature, the growth of α-Sn is done on III-V and II-VI substrates, leading to compressive strain. For α-Sn being a zero-gap semiconductor when being unstrained opens up new possibilities to explore when such material is grown by introducing strain. It has been seen in the literature that when ultrathin layers of material are grown along with strain, it can open sizable bandgaps. It has been seen that 5nm films of α-Sn grown on CdTe (111) exhibited a trivial bulk gap of nearly 420 meV [48]. On the other hand,

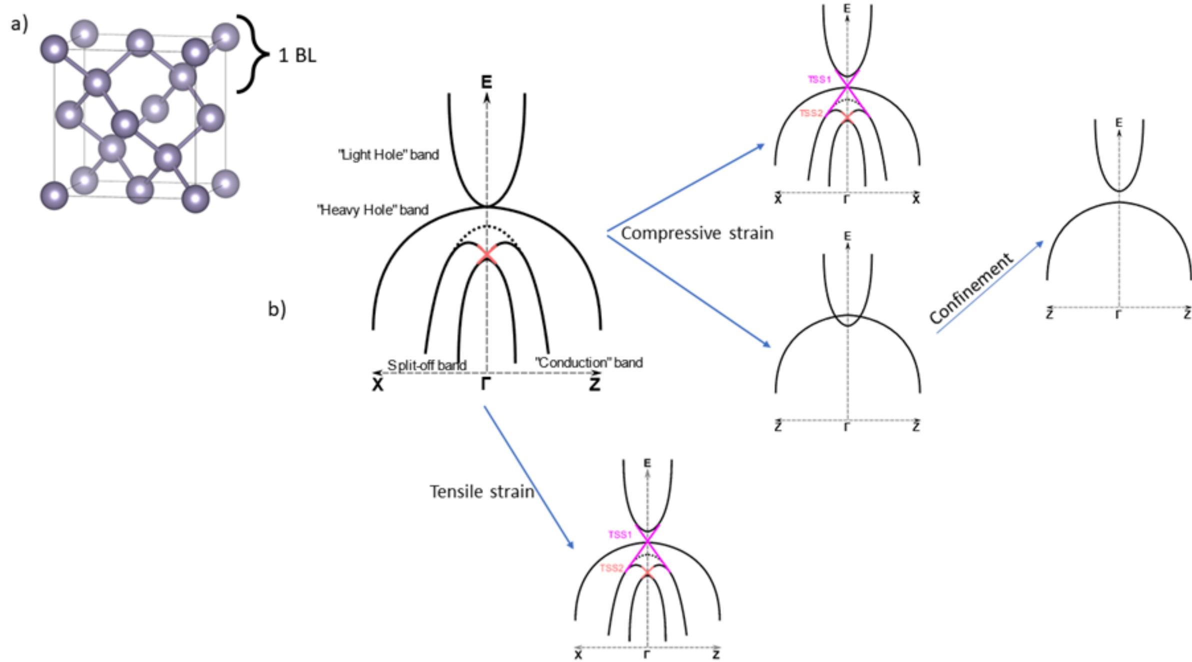

Figure 4.3: *a) The diamond crystal structure of α-Sn, the layer corresponding to 1 bilayer (BL) is shown. (b) A schematic of the band structure changes of -Sn. Biaxial compressive strain opens up a gap in the plane and band crossings out of the plane, forming a Dirac semimetal. Confinement by reducing film thickness gaps out the bulk Dirac crossings, forming a topological insulator. Alternatively, a topological insulator is formed by applying biaxial tensile strain.(credit- Aaron N. Engel)*

in the monolayer limit, films of a-Sn are predicted to have a nontrivial bandgap of about 0.1 eV [49].

It can be seen in Figure 4.2 that thick α-Sn grown on CdTe or InSb are Topological Dirac semi-metal whereas if the thickness of the material is lowered, a 3D Topological Insulator or a 2D Topological Insulator is expected. Bulk crystal of unstrained α-Sn is experimentally determined to be a zero-gap semiconductor. There also have been several theoretical calculations if bulk crystals are grown on larger lattice constant substrates it will be a 3D TI. If films are grown in the ultrathin limit, it is suggested to be 2D TI, but there is very little information about the ultrathin properties of α-Sn under tensile strain. This served as the main motivation for growing α-Sn on InSb under tensile

strain. Theoretical predictions show that the zero-gap semiconductor phase transitions to a Dirac semimetal (DSM) under epitaxial compressive strain and a topological insulator (TI) under epitaxial tensile strain as shown in Figure 4.3 [50], [51].

Another aspect of this project was to grow thin films of α-Sn by alloying them with germanium. The tensile strain can be induced by alloying the α-Sn with isovalent Ge (α-$Sn_{1-x}Ge_x$), which has a smaller lattice parameter. Hence, this alloying decreases the bulk alloy lattice constant, resulting in a tensile strained film when grown epitaxially on InSb. It might be seen by alloying enough Ge, that the properties of ultrathin tensile strained thin films can be studied for the first time.

The goal of this project was primarily to utilize strain to tune transport properties in α-$Sn_{1-x}Ge_x$ and determine it by magneto-transport measurement.

4.2.2 MBE growth

The α-Sn films studied here were grown using a modified VG V80 MBE growth system. All samples were grown on undoped (001)-oriented InSb substrates (WaferTech Ltd.). The oxide of the InSb(001) substrate was first removed by atomic hydrogen cleaning with a thermal cracker cell (MBE Komponenten). The samples were heated to 300°C and exposed to the atomic hydrogen for 30 minutes at a chamber pressure of 5×10^{-5} Torr. This resulted in the In-rich c(8×2)/4×2 surface reconstruction, as determined by reflection high energy electron diffraction (RHEED) [52].

The Sb-rich samples were prepared with constant monitoring of the reconstruction via RHEED along the [110] while referencing the InSb(001) surface reconstruction phase diagram [52,53]. The substrate temperature was ramped continuously from 373 K through the following transitions to the final annealing temperature. Near 550 K, the c(8×2) surface was dosed with approximately 0.75 ML Sb until the c(8×2) just fades to the

p(1×1) reconstruction. At higher temperatures, the reconstruction transitions to the c(4×4) and, starting a few degrees below the c(4×4)/a(1×3) transition (approximately 643K), was exposed to an Sb_4 flux continuously. The sample was then annealed under an Sb_4 overpressure 40- 60 K above this transition point for at least 30 minutes. The sample was then cooled quickly down back through the a(1×3)/c(4×4) transition to achieve the final c(4×4) reconstruction. α-Sn was then grown on each sample at a rate of 0.5 BL/min at "room" temperature. The growth of the α-Sn samples was done by my group member Aaron N. Engel. The first paper on the growth and characterization has been published [54].

In this thesis, the characterization of these grown materials is the main focus through the fabrication of Hall Bars and doing low-temperature magnetotransport measurements in a cryogenic measurement system.

4.3 Fabrication of Hall Bars

One of the main properties of Sn is that it can change its phase from α to β at 286.2K. So, it is crucial in the processing that there should be no introduction to heat.

So, the major challenges faced during processing were two - no heating while baking during lithography, and finding the correct etch chemistry for etching the Sn as well as InSb to form a MESA. In this section, the process of how the Hall bars were fabricated will be discussed. The fabrication process flow for the Hall Bars is shown in Figure 4.4.

4.3.1 Optical Lithography without baking

Any process of writing a pattern on a sample requires lithography, and for every lithography, soft baking of the photoresist is very essential for hardening the photoresist and also allows writing sharp patterns on the sample. This soft bake usually is done at

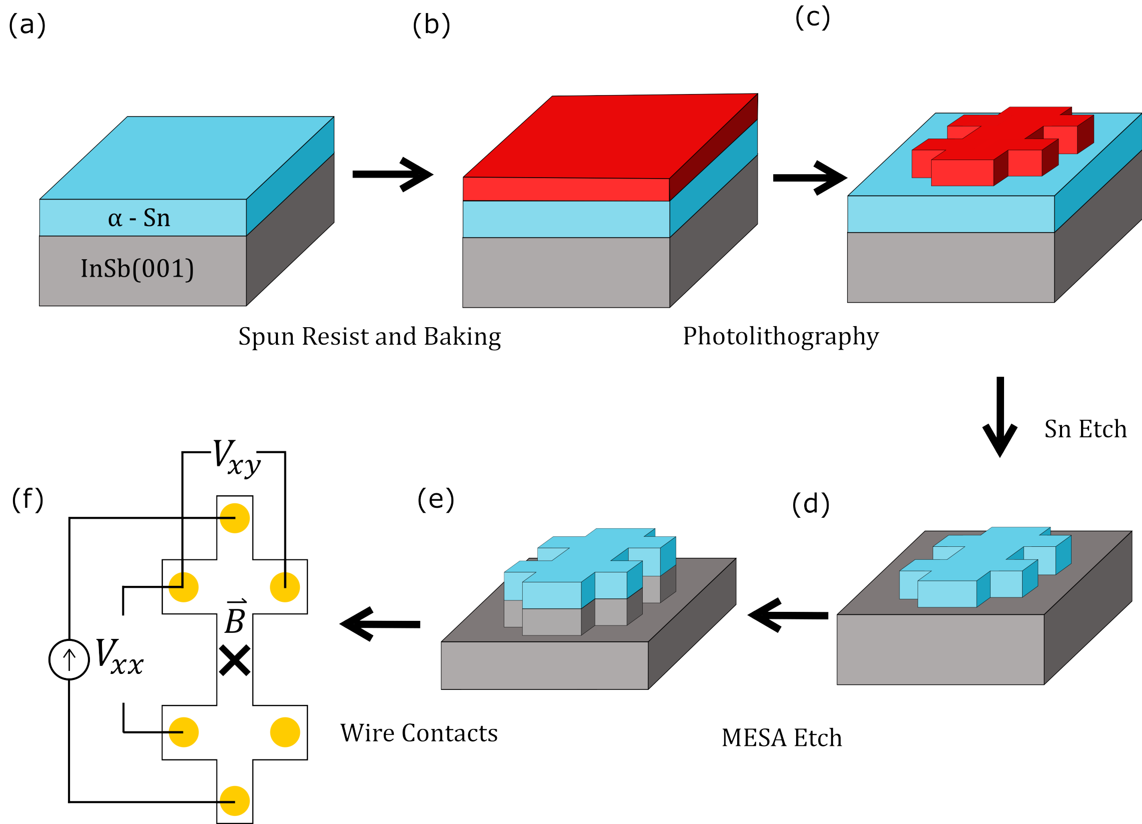

Figure 4.4: **Fabrication Process Flow** *(a) MBE grown α-Sn on InSb (b) sample after coating with photoresist and vacuum baking the resist (c)lithography showing the Hall bar geometry (d) after Sn-etch (e) forming MESA by etching InSb. (f) wire contacts for transport measurements.*

a temperature of 95°C - 100°C. So, for the processing of Hall bars on α-Sn, this was a major challenge as at any point nucleation of β-Sn can start.

"Vacuum baking" instead of soft baking the photoresist served as the solution. As it is known, soft baking is typically used to evaporate solvents from the photoresist, forming a firm layer that enhances adhesion and uniformity. When vacuum baking is used instead, the process occurs under reduced pressure, causing the solvents to evaporate without heating due to lower vapor pressure. This rapid evaporation accelerates the solidification of the photoresist, reduces air bubble formation, and can improve the layer's surface uniformity and adhesion by minimizing internal stress. Additionally, vacuum

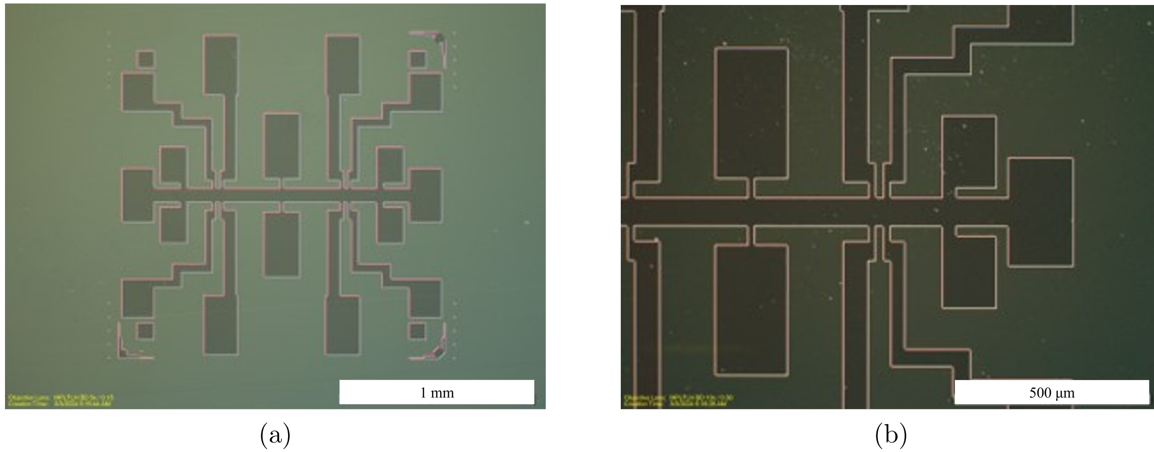

(a) (b)

Figure 4.5: **Photolithography** *(a,b) Hall bar after photolithography with 3 hours of keeping in air and 1 hour of vacuum treatment.*

baking reduces particulate contamination, keeping the photoresist surface cleaner. These factors contribute to the effectiveness of vacuum baking in the process, making it a viable alternative to soft baking.

Several iterations were done to figure out the optimal time for the vacuum treatment. Finally, it was seen that 3 hours of keeping the sample in ambient air and 1 hour and 15 minutes of baking in vacuum resulted in sharp patterns as shown in Figure 4.5.

4.3.2 Etch Calibrations

The next challenge faced was to figure out the etch chemistry for α-Sn which would give sharp patterns for the Hall bars. In literature, there have been few suggestions for the etch chemistry. For such suggestions, it is important to see if the solution would undercut the patterns, or give sharp corners.

InSb etch

To form the MESA for the Hall bars, it is essential to find the etch solution for InSb. For that series of test runs were done on InSb and alloys of $In_{1-x}Al_xSb$ to figure out the

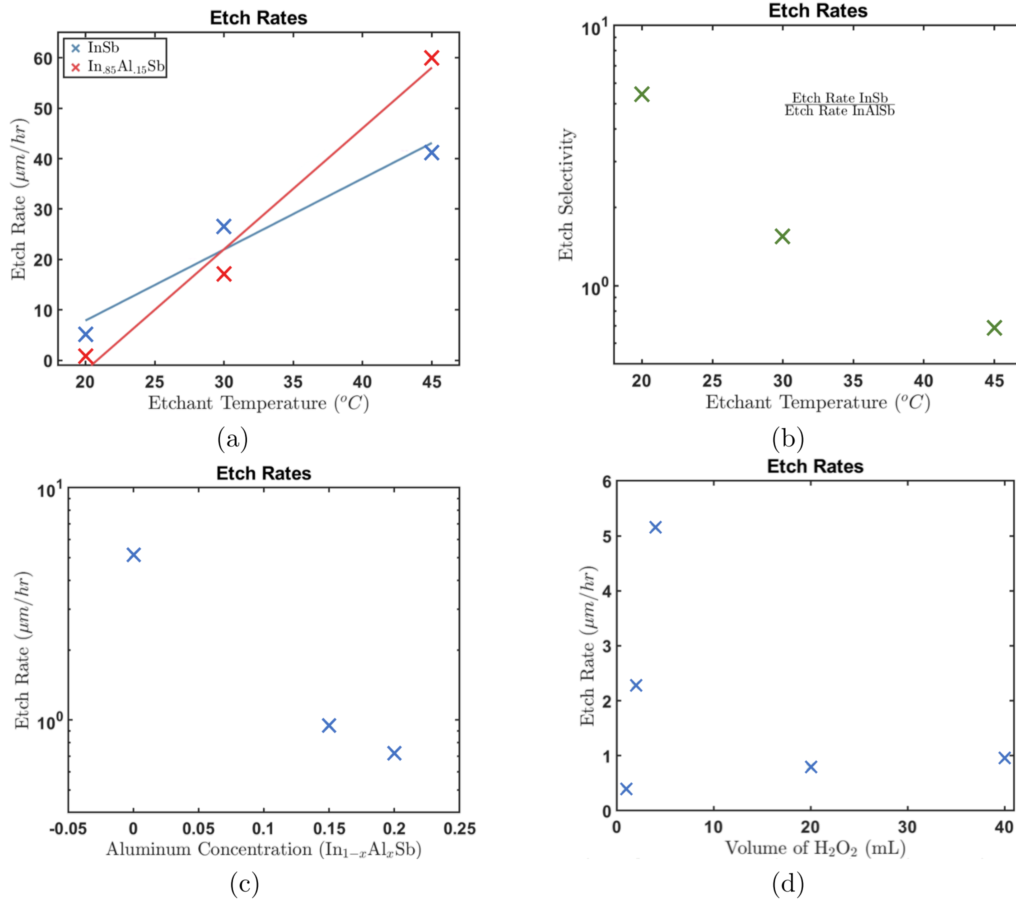

Figure 4.6: **InSb etch calibrations** - *(a)Etch rate vs etchant temperature of InSb and* $In_{0.85}Al_{0.15}Sb$ *(b)Etch Selectivity of InSb and* $In_{0.85}Al_{0.15}Sb$ *vs. etchant temperature (c) Etch rate vs. the Aluminum concentration (d) Etch rate of InSb vs the volume of* H_2O_2 *used.*

etch rate as well as the etch selectivity. A solution of a mixture of Citric Acid($C_6H_8O_7$) and H_2O_2 was considered for the etching. For the tests, etch was done for different temperatures as well as the H_2O_2 concentration. Figure 4.6(a) shows the changes in etch rate for InSb as well as $In_{0.85}Al_{0.15}Sb$ as a function of temperature follows a linear trend, where the one for $In_{0.85}Al_{0.15}Sb$ shows a steeper slope. The etch selectivity is also seen in Figure 4.6(b), which shows a steady decrease as the temperature is increased to 45°C. For this etch, a solution of 50:1 $C_6H_8O_7$:H_2O_2 was used.

Figure 4.6(c), shows how changing the Aluminium concentration changed the etch

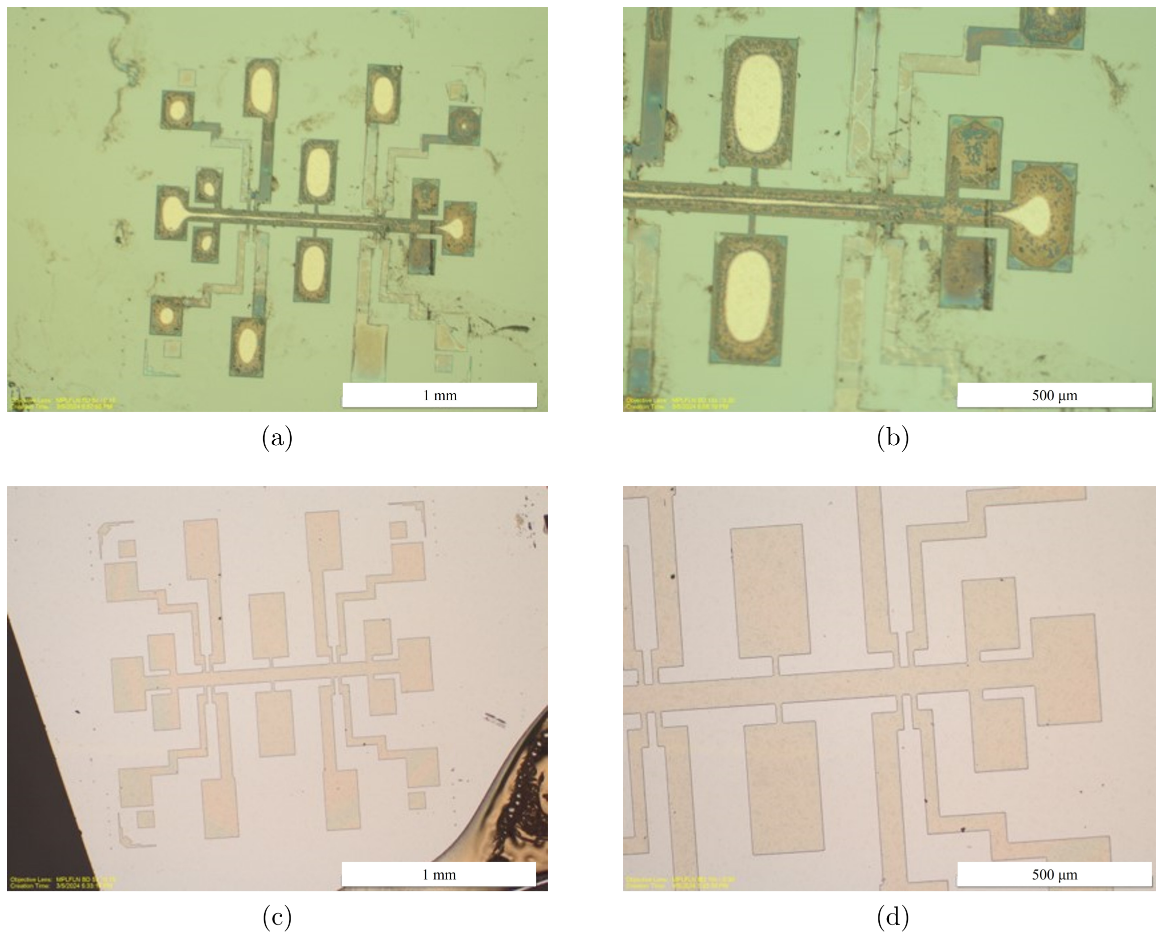

(a) (b) (c) (d)

Figure 4.7: **α-Sn Etch Calibrations** - *(a-b) Hall bar after etching with HCl:H_2O_2:H_2O (c-d) Hall bar after etching with HCl:H_2O*

rate. This potentially suggests if Al concentration is increased to 0.3% or higher the selectivity can dramatically increase the selectivity considering this is a log plot. In Figure 4.6(d), it was seen for different volumes of H_2O_2, the etch rate changed. The maximum etch rate was found as the $C_6H_8O_7$:H_2O_2 volume was increased to 4 ml, while as we increased the H_2O_2 volume to 20ml and 40ml consecutively the etch rate was lowered.

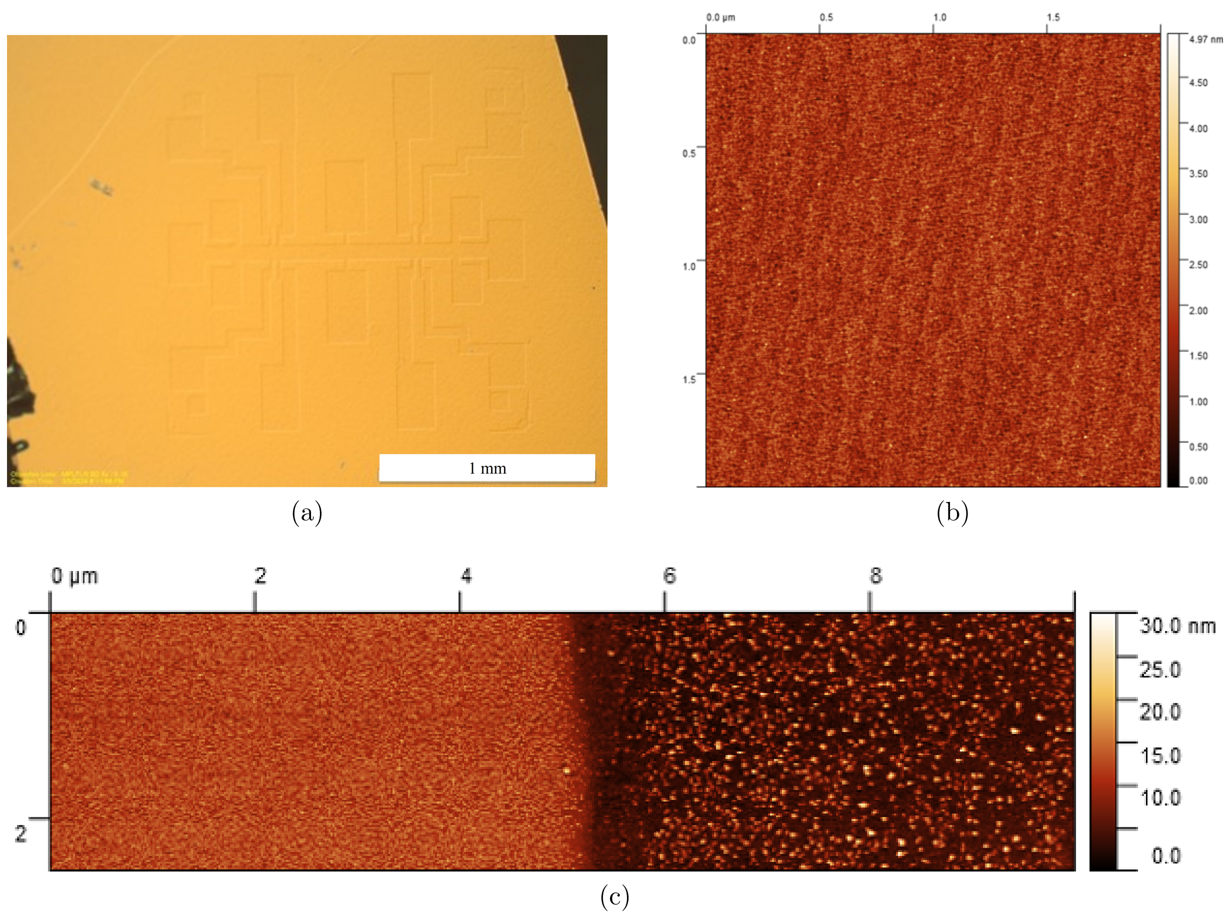

Figure 4.8: **α-Sn Etch Calibrations** - *(a) after 2 minutes of etch using 3:10 HCl:H_2O (b) AFM before processing (c) AFM after processing.*

α-Sn Etch

For the first iteration process, two different solutions were chosen - HCl:H_2O_2:H_2O and HCl:H_2O. For the first solution of HCl:H_2O_2:H_2O, a ratio of 4:1:40 was used and etched for 30 secs. The sample after etch seems destroyed with the H_2O_2 affecting the photoresist and also there being a large undercut as seen in Figure 4.7(a). Next the HCl:H_2O with a concentration ratio of 3:10 was used for 2 mins. As seen in Figure 4.7(b), the sample remained unaffected with no undercut and sharp sidewalls. As we stripped off the photoresist as it was seen the Sn layer was not etched fully, so apparently

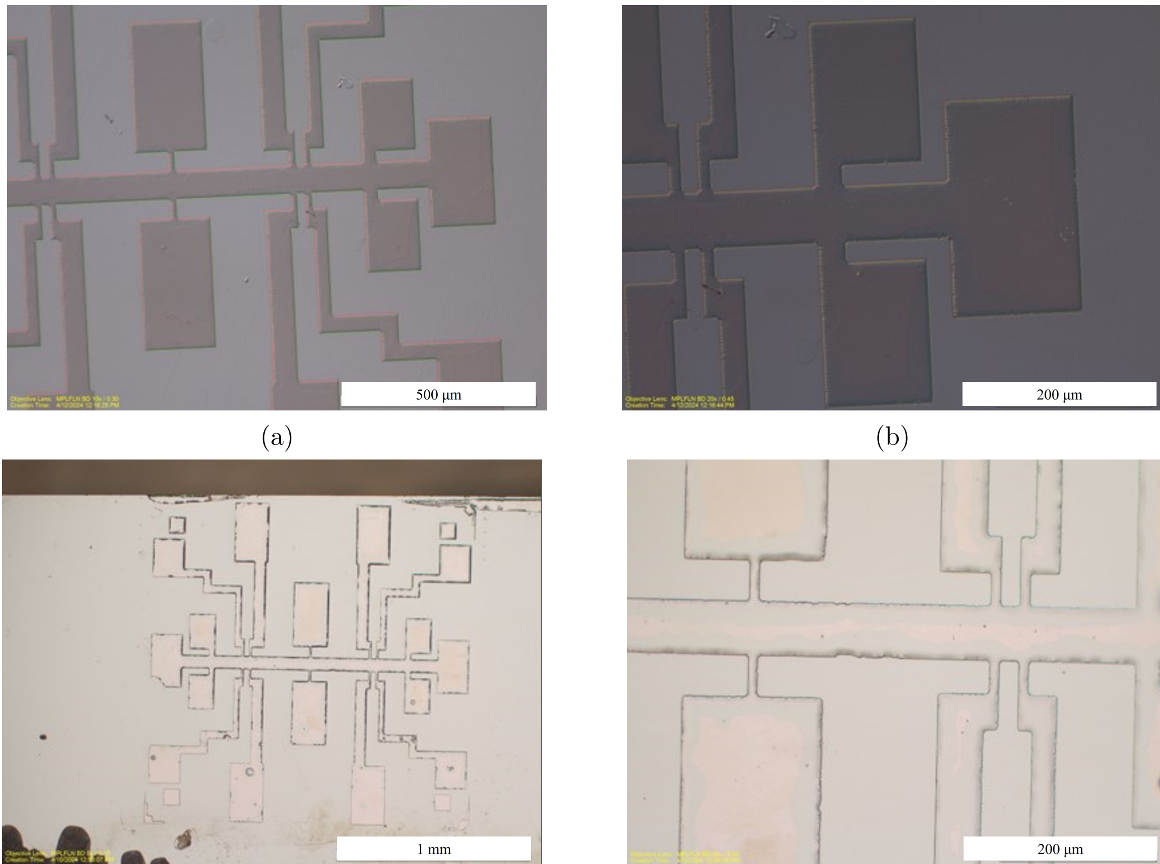

Figure 4.9: α**-Sn Etch Calibrations** - *(a-b) Undercut while using 1:1 HCl:H_2O (c) Hall Bar after MESA etch (d) α-Sn on the Hall bar etched away after due to major undercut.*

the etch rate was very slow. It can be seen in Figure 4.8(a) the hall bar is barely visible. It was important to see if the α-Sn after processing was showing any changes in surface morphology,i.e. if there was any nucleation of β-Sn. To check this, Atomic Force Microscopy(AFM) was used to see the surface morphology before processing as seen in Figure 4.8(b). This was then matched with the AFM of the α-Sn after processing as seen in Figure 4.8(c). It can be seen in the left side of Figure 4.8(c) that the Sn which was protected by photoresist did not change its phase as there has been no nucleation and on the right it is seen where the sample was being etched.

Next, as the etch rate was very slow, the concentration of HCl:H_2O changed abruptly

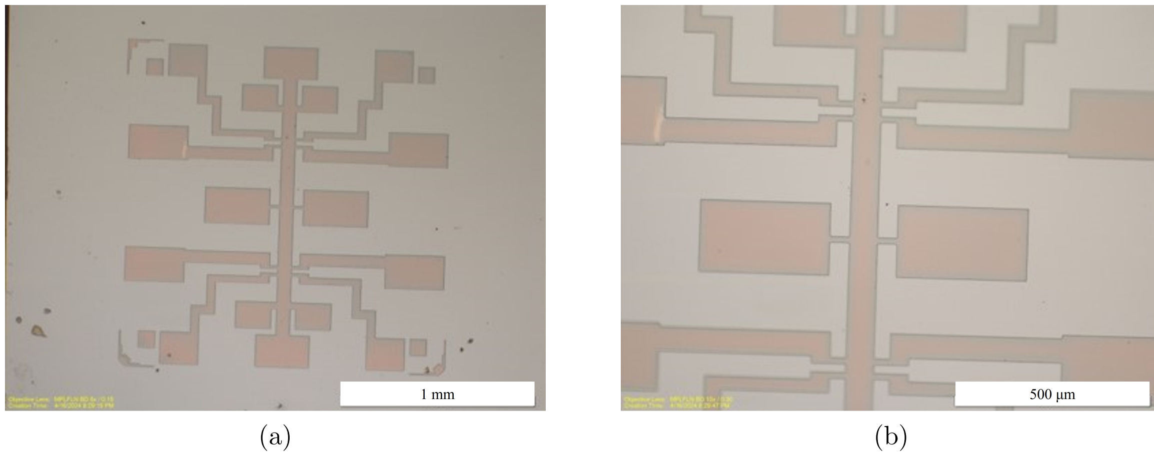

(a) (b)

Figure 4.10: **α-Sn Etch Calibrations** - *(a-b) Hall bars showing no undercut issue after using 2:3 HCl:H_2O.*

to 1:1 from 3:10. After etching the sample it was seen that the Sn was etched fully. Figure 4.9(a-b), the resist has an under-etch, which leads to the etching of Sn. Now, to figure out the whole etching procedure, the InSb was also etched using the etch chemistry as shown in Figure 4.6(a). A concentration ratio of 50:1 of Citric:H_2O_2 was used. It can be seen in Figure 4.9(c-d) that the α-Sn was etched due to an undercut.

Next, after many iterations of using different concentrations, 2:3 HCl:H_2O was used for the α-Sn etch. As seen in Figure 4.10, the photoresist did not show any undercut as well as the patterns had sharp edges. The etch rate for 56BL of α-Sn was found to be around 6.5nm/min. Though it was seen later, the etch rate also depends upon how much alloying is done with Germanium. A trend was seen whereas the Germanium alloy ratio was increased the etch rate went down.

As seen in Figure 4.6(a), the highest etch rate was seen for a concentration ratio of $C_6H_8O_7$:H_2O_2 of 50:1. The sample was etched for 3 minutes to find an etch depth of (400nm). It can be seen in Figure 4.11 that the Citric acid was etching the Sn again showing a shape of concentric circles at the edges.

It has been seen in literature that the H_2O_2 concentration can affect the etching of

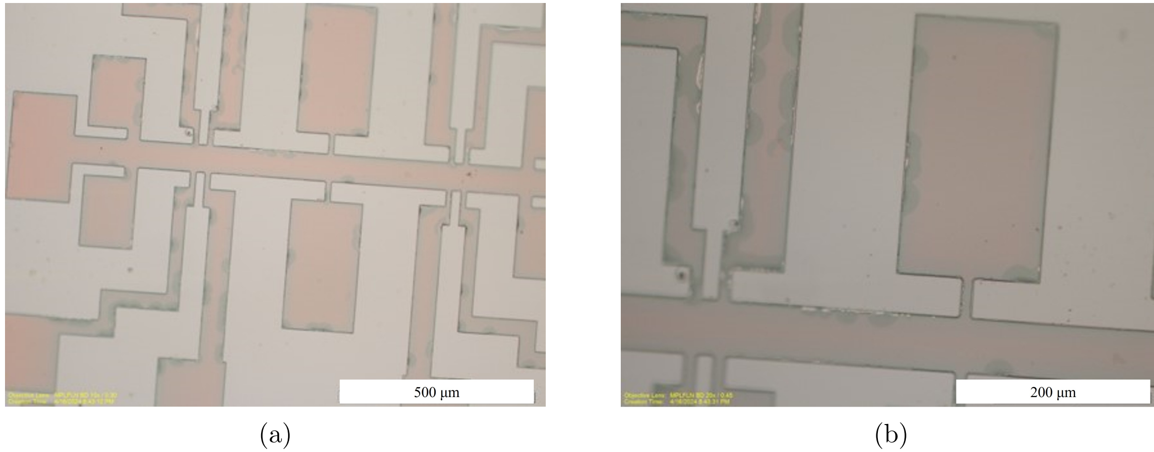

(a) (b)

Figure 4.11: *(a)Undercut issue using 50:1 $C_6H_8O_7$:H_2O_2 for InSb etch (b) α-Sn etched in concentric circular undercut patterns.*

α-Sn, but if the concentration is increased, it can lead to the formation of Stannous oxide which doesn't etch with Citric acid [55, 56]. For this reason, the H_2O_2 concentration was increased to 40ml from 4ml, resulting in the etch ratio of $C_6H_8O_7$:H_2O_2 to be 200:40. This showed great results as seen in Figure 4.12(a,b). The figure shows the etch results without the PR being stripped off. There was no undercut of the resist which was seen in Figure 4.11. As the PR was stripped off, the final device was obtained in Figure 4.12(c,d).

4.4 Results and Discussion

The hall bars thus fabricated on α-Sn were characterized using the Quantum Design PPMS. Four different samples were fabricated using different germanium compositions of, 3%, 5%, 7%, and 10%.

4.4.1 Temperature Dependence

The layer structure of the measured samples is depicted in Figure 4.13. The longitudinal resistance, R_{xx} was measured while the sample was cooled from room temperature

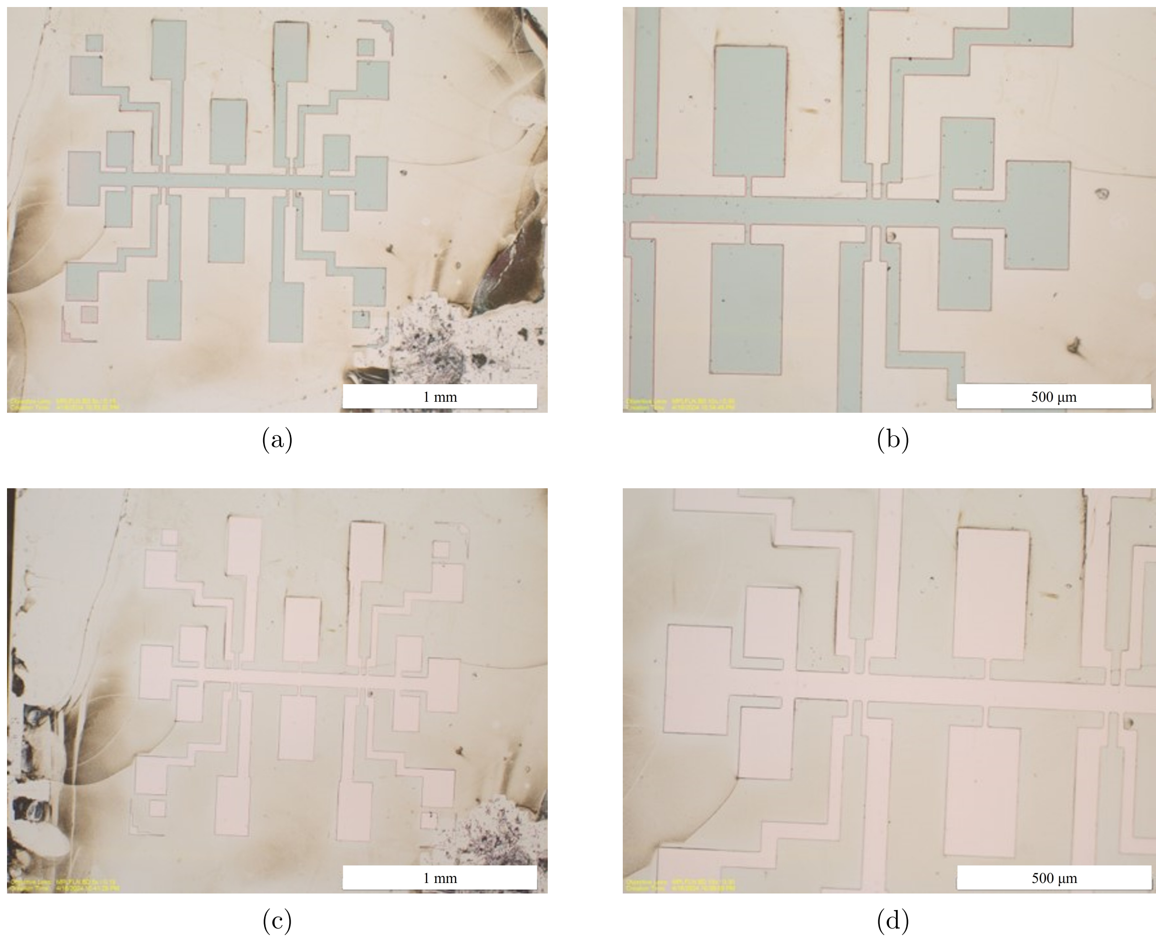

(a) (b) (c) (d)

Figure 4.12: **Final Device** - *(a-b) Final device after both α-Sn and InSb etch (c-d) after PR strip off showing the final Hall bar.*

to 2K. As the temperature of the device is reduced, the ohmic resistance initially increases exponentially with temperature. It was seen at a temperature of around 160K, the resistance decreased to 40K and then again increased. Starting at room temperature, the sample initially exhibits decreasing resistance as it cools. This is due to the reduction in lattice vibrations, which typically scatter charge carriers, improving their mobility. As the temperature drops further into the extrinsic region, the resistance reaches a minimum since impurities can efficiently supply charge carriers. However, cooling the sample even more leads to the freeze-out region, where impurity levels can no longer excite electrons

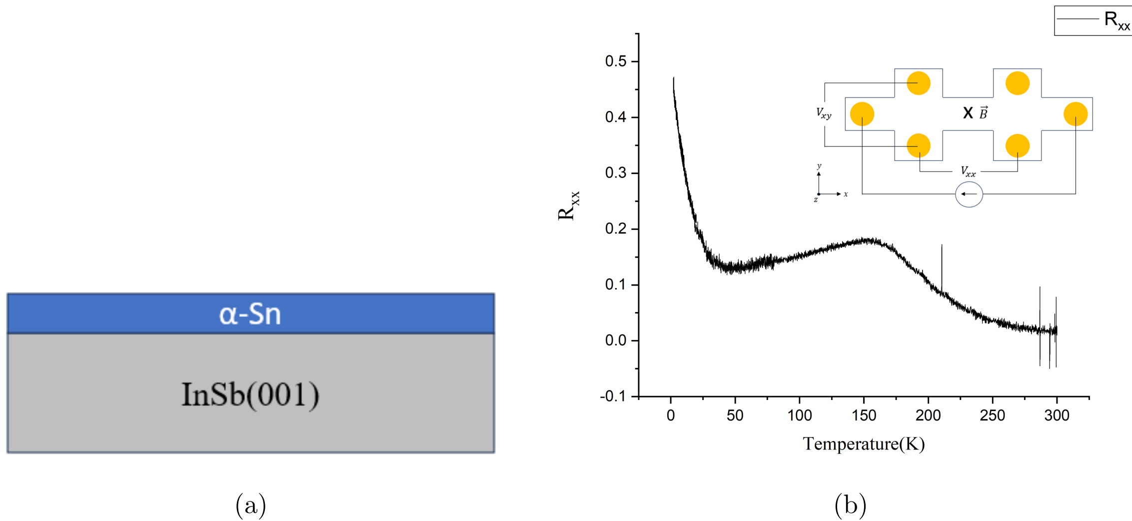

Figure 4.13: *(a) Schematic representation of α-Sn grown on InSb. (b) Temperature dependence of the longitudinal resistance. Inset depicts hall bar geometry.*

into the conduction band due to insufficient thermal energy, causing resistance to rise sharply again. As the temperature continues to decrease, intrinsic carrier generation is severely reduced, leading to a further increase in resistance. This behavior is mostly due to the parallel conduction channels through the InSb. InSb being a small bandgap material, it is very hard to freeze-out the carriers, so there can be a large contribution from the InSb substrate. This has also been reported in here [57].

4.4.2 Magnetotransport Analysis

Longitudinal and transverse resistance measurements for the 56 BL α-Sn films grown on InSb(001) are presented in Figure 4.14. Shubnikov–de Haas oscillations are evident in both geometries, as illustrated in Figure 4.14(a) for a sample with 3% Germanium composition. Similar characteristics have been observed previously, as reported in [54]. Figure 4.14(b) shows the magnetoresistance for a sample with 10% Germanium concentration. The peaks seem symmetrical which opposes the usual asymmetry in the Hall

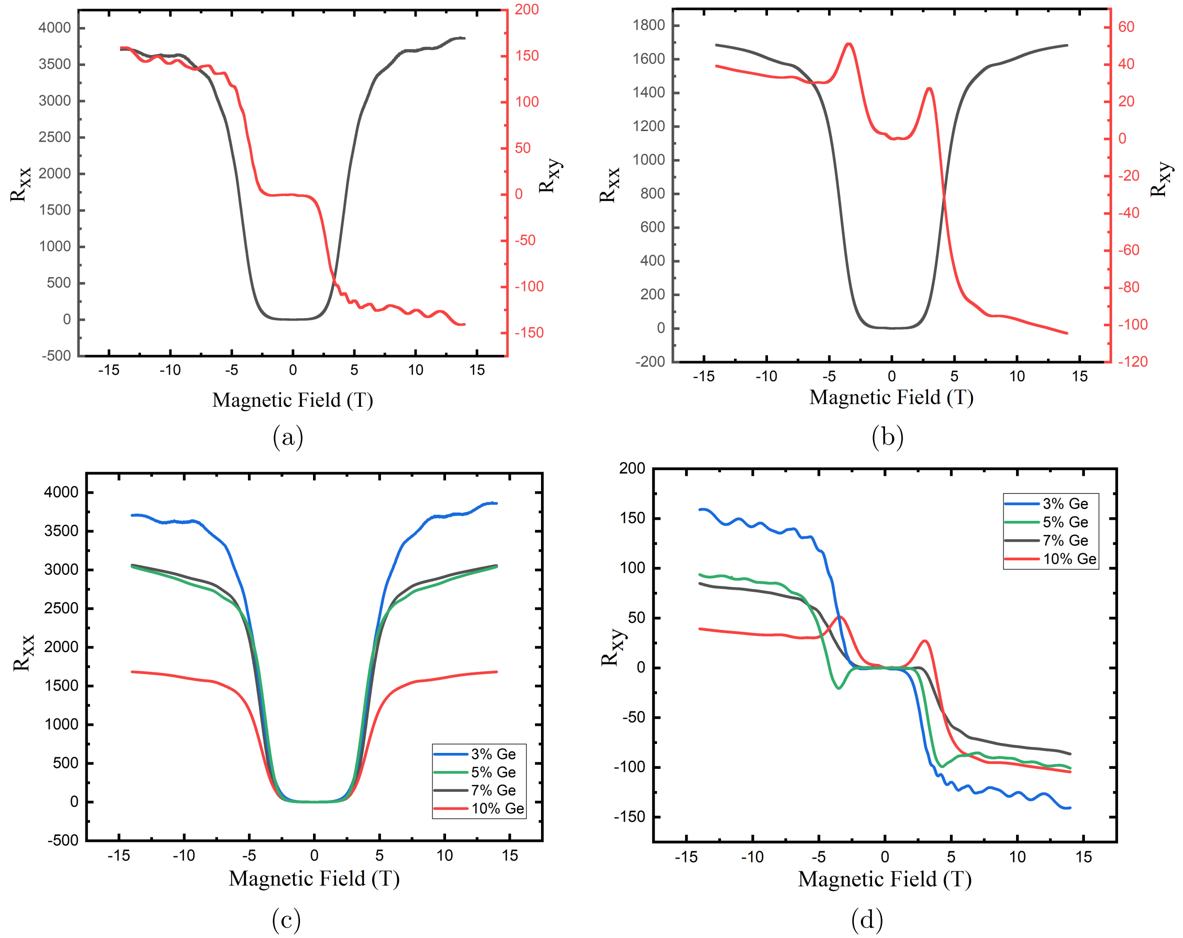

Figure 4.14: *(a,b) Longitudinal and transverse resistivity taken with sample cooled to 2 K vs. magnetic field intensity for two different germanium compositions - 3% and 10%. (c,d) Longitudinal and transverse resistivity vs. Magnetic field of four different samples with varying germanium composition.*

data. So, this might be an influence of multiple carriers affecting the Hall data or might be seen as an artifact from the measurement that cannot be explained without more information. Additionally, the longitudinal and transverse resistance of samples with varying Germanium compositions are depicted in Figures 4.14(c) and 4.14(d), respectively.

In the longitudinal geometry, we observe a sharp increase in the resistance at an applied field of around 4T as seen in Figure 4.14(c). This results from the established magnetic-field-induced metal-insulator transition in InSb [58]. The behavior of freeze-out

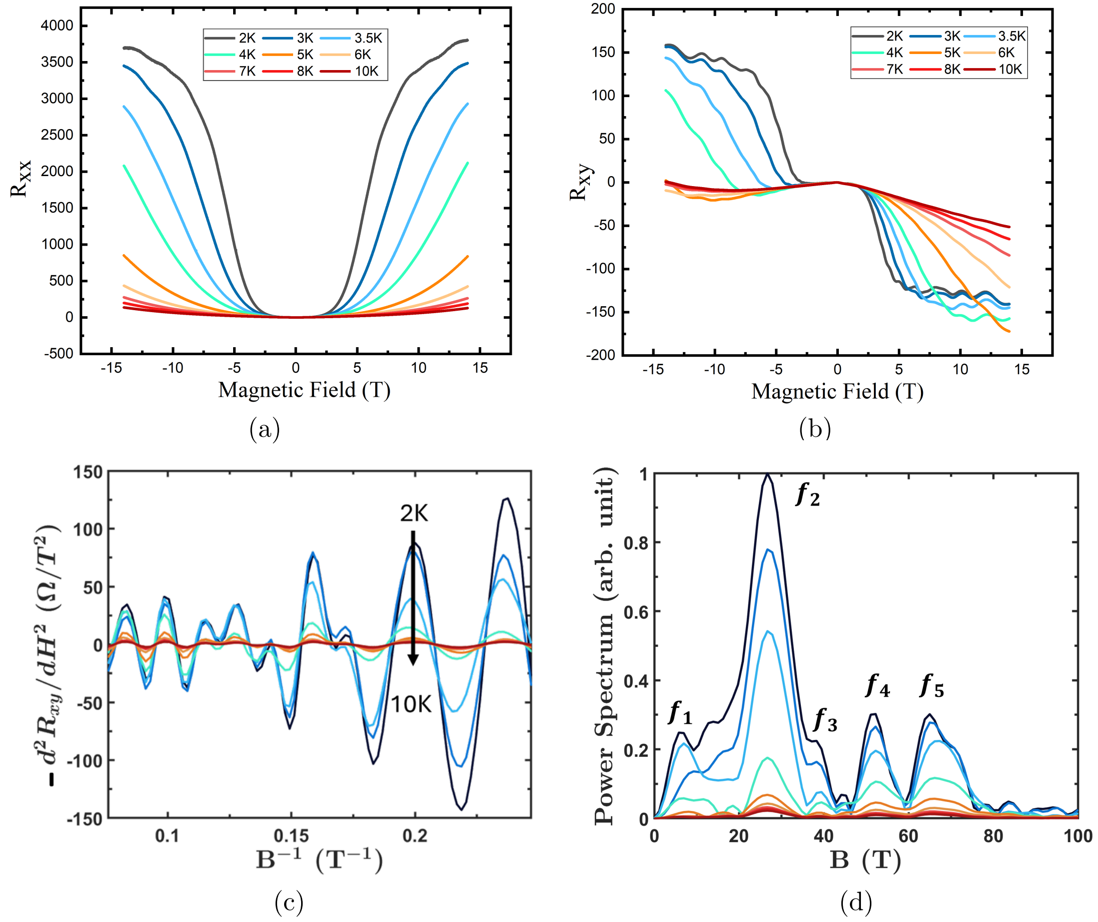

Figure 4.15: *(a,b) Longitudinal resistance and Transverse resistance traces as the temperature of the sample is changed from 2K to 10K (c) Second derivative of the transverse resistance (R_{xy}) vs inverse of the magnetic field (d) FFT of the presented region.*

in InSb is extremely sensitive to absolute dopant concentrations [59].

In Figure 4.15(a,b), resistance measurements for both longitudinal (R_{xx}) and transverse (R_{xy}) were recorded across a range of temperatures from 2 K to 10 K. As temperatures were varied, the magnetic field was also adjusted from -14 T to +14 T. At the cooler end of the temperature spectrum, a higher number of overlapping oscillations were noted. The amplitude of these oscillations diminished with an increase in temperature, attributed to the Fermi function broadening, which induces a greater degree of energy

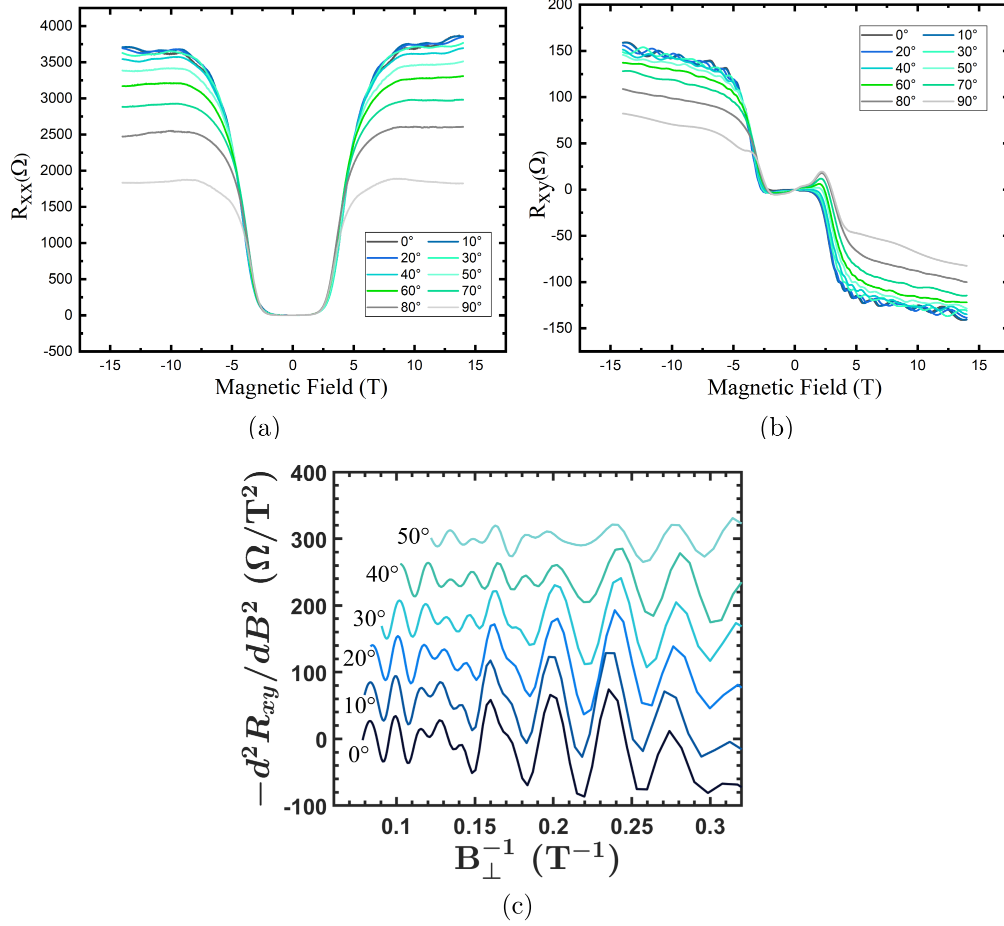

Figure 4.16: *(a,b) Longitudinal resistance and Transverse resistance of* 3%*-Ge* α*-Sn traces as the angle of sample is changed from* $\vec{B}\angle\hat{n} = 0°$ *to* $90°$ *(c) Negative of the second derivative of transverse resistance* (R_{xy}) *plotted against the perpendicularly applied magnetic field.*

averaging near the Fermi energy.

To isolate these oscillations, the raw data was refined by taking the second derivative of the resistance with respect to the field. Further analysis involved plotting the second derivative of the resistance spectra (R_{xy}) against the reciprocal of the magnetic field (1/B). The Shubnikov-de Haas (SdH) oscillations, inherently periodic in 1/B, facilitated the determination of the oscillation frequency.

In Figure 4.15(c), the decrease in oscillation amplitudes is attributed to thermal

effects. An FFT (Fast Fourier Transform) was performed on each dataset to identify the oscillation frequencies. A broad range of inverse field values, from 0.07 T^{-1} to 0.30 T^{-1} (equivalent to a magnetic field range from 3.3 T to 14 T), was used. The FFT results, depicted in Figure 4.15(d), reveal five distinct peaks, designated as f_1 through f_5. These peaks correspond to frequencies of f_1 = 5.8T, f_2 = 26.7 T, f_3 = 37.1 T, f_4 = 52.2 T, and f_5 = 64.9 T. The dimensionality of the transport channels is yet to be figured, one would expect the transport in InSb to be 3D whereas the transport in α-Sn should be 2D. Concurrently, ongoing investigations into samples with different Germanium concentrations aim to elucidate variations in transport mechanisms.

Figure 4.16(a) illustrates how the longitudinal resistance (R_{xx}) of a sample varies with magnetic field orientation at a constant temperature of 2K. During these measurements, the sample's surface normal, $\hat{n}$, was incrementally rotated relative to the direction of the magnetic field, $\vec{B}$. For a 2D Fermi surface, the SdH oscillations are expected to be influenced primarily by the component of the magnetic flux perpendicular to the surface. Consequently, the oscillation frequency should vary as $f_i \propto 1/\cos(\theta)$. Figures 4.16(a) and (b) display the magnetoresistance data at various angles between $\hat{n}$ and $\vec{B}$. The data show a decrease in oscillation intensity as the angle increases.

To investigate the dimensionality of the oscillations and pinpoint their origins at large angles, the inverse perpendicular magnetic field's relationship to the negative second derivative of the transverse resistance was graphically represented, as seen in Figure 4.16(c). The perpendicular magnetic field, denoted as $B_\perp$, is determined by the equation $B_\perp = \vec{B} \cdot \hat{n}$, with $\hat{n}$ being the surface normal. Oscillations associated with 2D transport mechanisms depend entirely on the component of the magnetic field that is perpendicular to the film's surface, which means the peak and trough locations should stay consistent for various $\vec{B}\angle\hat{n}$ values when plotted against $B_\perp$. Figure 4.16(c) demonstrates that these peak and trough locations do not shift at lower fields despite changes in the angle,

indicating a 2D transport origin. To confirm this interpretation, it is crucial to analyze how the oscillation frequencies adjust with angle, expecting a 2D channel to show a frequency relation of $f_i \propto 1/\cos(\theta)$. Further investigations are underway to substantiate these observations.

4.5 Conclusion

In this chapter, the growth of ultrathin α-$Sn_{1-x}Ge_x$ on InSb(001) was done with tensile strain. A hall bar geometry was considered for the characterization of the grown samples. α-Sn being able to change its phase when samples are exposed to higher temperatures, low-temperature processing is necessary to fabricate the hall bars. Vacuum baking was used instead of soft baking for photolithography Also, the etch chemistry of the α-Sn and InSb was found to form the hall bars. The magnetotransport measurements of the samples have been also demonstrated for samples having varying germanium composition. Preliminary analysis of data for the temperature dependence and the angular dependence of the Shubnikov-de Haas oscillations have also been shown.

Chapter 5

Summary and Outlook

The main goal of this thesis is to make advancements in the field of Quantum Computing through exploring its branches. Materials and structures have been studied for Superconducting and Topological Quantum Computing respectively. Growth, fabrication and characterization of these devices have been explained.

Firstly, the *in-situ* growth of Josephson Junction is demonstrated. Growth of structures using shadow masks helps in immense purity of the crystal structure which is of utmost importance especially when it comes to Superconducting qubits. The fabrication of such shadow mask and using them to grow junctions is demonstrated for Ta with Low temperature-MBE(LT-MBE). One of the device showed promising characteristics which can be further investigated.

Another branch that this thesis explores is the application of α-Sn in topological quantum computing. For the first time, utilizing the Ge alloying, α-Sn has been grown to have tensile strain. Low-temperature processing (no heating) has been done to fabricate Hall bars which allows us to magnetotransport measurements. Shubnikov-de Haas oscillations have been seen for the samples and also it's temperature and angular dependence are shown. Though only preliminary analyses of the data has been done, more

analysis of the data is required to understand the effect of Ge alloying in the α-Sn. For future work, the magnetotransport measurements should be analyzed more to find if α-$Sn_{1-x}Ge_x$ serves as a topological insulator. After these analyses, growth of Sn and α-$Sn_{1-x}Ge_x$ on $In_{1-x}Al_xSb$ can be done. This serves as a barrier for back gating the samples to tune the sign and density of the free carriers. In addition, the VBO between Sn and InSb is likely different than that of Sn and AlSb. By changing the Al composition x, we could potentially tune the valence band offset (VBO) as well. These approaches could potentially help reduce the number of bulk carriers in the system.

Appendix A

Fabrication Recipe - Shadow Mask

A.1 Front Side Patterning

1. Out of the box Si(001) wafer with LPCVD grown 200nm Si_xN_y.
2. Clean the wafer using oxygen plasma for 15 secs.
3. Soak the wafer in HMDS for 40 seconds and spin for 1 minute.
4. Bake at 100°C for 60 seconds.
5. Spin AZ4110 at 4000 rpm for 60 seconds.
6. Bake at 95°C for 60 seconds.
7. Do the MLA (Dose - 200 $\mu C/cm^{-2}$) for the front side patterns and markers.
8. Develop for 75 seconds in AZ400K 1:4.
9. Open up patterns in oxygen plasma for 15 seconds.
10. Dry etch – O_2 clean for 5 mins, CF_4/O_2 coat for 2 mins, CF_4/O_2 etch for 4 mins, O_2 clean for 5 mins.

11. Clean with O_2 plasma for 2 minutes.

12. Rinse and clean the photoresist with Acetone and IPA.

13. Use O_2 plasma for 5 minutes.

14. Rinse with IPA and DI water.

15. Make sure the wafer is clean.

16. Use O_2 plasma for 15 seconds.

17. PECVD LSNitride V3 for 10 minutes.

18. Soak 40 seconds in HMDS and spin for 1 minute

19. Bake at 100C for 60 seconds.

20. Spin AZ4110 at 4000 rpm for 60 seconds.

21. Bake at 95°C for 60 seconds.

A.2 Backside Patterning

1. Clean it with O_2 plasma until clean.

2. Soak 40 seconds in HMDS and spin for 1 minute

3. Bake at 100C for 60 seconds.

4. Spin AZ4110 at 4000 rpm for 60 seconds.

5. Bake at 95°C for 60 seconds.

6. MA6 Backside Alignment for Markers.

7. Develop for 60 seconds in AZ400K1:4.
8. Do MLA(Dose - 300 μC/cm^{-2} for the backside pattern.
9. Develop for 60 seconds in AZ400K1:4.
10. CF_4/O_2 etch for 12 minutes to open up the mask and etch. And then O_2 plasma for 2 minutes.
11. Rinse with Acetone, IPA, and DI water.
12. KOH Etch at 87°C for 8 hours.
13. BHF etch for 3 minutes and 30 seconds.
14. Back to KOH etch till the patterns come through.
15. Clean the mask with IPA and DI water.

Bibliography

[1] R. Schaller, *Moore's law: past, present and future*, *IEEE Spectrum* **34** (1997), no. 6 52–59.

[2] N. D. Mermin, *Quantum Computer Science: An Introduction*. Cambridge University Press, 2007.

[3] K. v. Klitzing, G. Dorda, and M. Pepper, *New method for high-accuracy determination of the fine-structure constant based on quantized hall resistance*, *Phys. Rev. Lett.* **45** (Aug, 1980) 494–497.

[4] J. Moore, *The birth of topological insulators*, *Nature* **464** (03, 2010) 194–8.

[5] C. L. Kane and E. J. Mele, *Topological order and the quantum spin hall effect*, *Physical Review Letters* **95** (Sept., 2005).

[6] L. Fu, C. L. Kane, and E. J. Mele, *Topological insulators in three dimensions*, *Phys. Rev. Lett.* **98** (Mar, 2007) 106803.

[7] M. Z. Hasan and C. L. Kane, *Colloquium: Topological insulators*, *Rev. Mod. Phys.* **82** (Nov, 2010) 3045–3067.

[8] X.-L. Qi and S.-C. Zhang, *Topological insulators and superconductors*, *Rev. Mod. Phys.* **83** (Oct, 2011) 1057–1110.

[9] L. Fu and C. L. Kane, *Topological insulators with inversion symmetry*, *Phys. Rev. B* **76** (Jul, 2007) 045302.

[10] Y. Xu, B. Yan, H.-J. Zhang, J. Wang, G. Xu, P. Tang, W. Duan, and S.-C. Zhang, *Large-gap quantum spin hall insulators in tin films*, *Phys. Rev. Lett.* **111** (Sep, 2013) 136804.

[11] T. Grover, D. N. Sheng, and A. Vishwanath, *Emergent space-time supersymmetry at the boundary of a topological phase*, *Science* **344** (2014), no. 6181 280–283.

[12] E. Majorana, *Teoria simmetrica dell'elettrone e del positrone*, *Il Nuovo Cimento* **14** (Apr., 1937) 171–184.

[13] H. Zhang, D. E. Liu, M. Wimmer, and L. P. Kouwenhoven, *Next steps of quantum transport in majorana nanowire devices*, *Nature Communications* **10** (Nov., 2019).

[14] A. Y. Kitaev, *Unpaired majorana fermions in quantum wires*, *Physics-Uspekhi* **44** (oct, 2001) 131.

[15] A. Kitaev, *Fault-tolerant quantum computation by anyons*, *Annals of Physics* **303** (2003), no. 1 2–30.

[16] C. Nayak, S. H. Simon, A. Stern, M. Freedman, and S. Das Sarma, *Non-abelian anyons and topological quantum computation*, *Rev. Mod. Phys.* **80** (Sep, 2008) 1083–1159.

[17] V. Mourik, K. Zuo, S. M. Frolov, S. R. Plissard, E. P. A. M. Bakkers, and L. P. Kouwenhoven, *Signatures of majorana fermions in hybrid superconductor-semiconductor nanowire devices*, *Science* **336** (2012), no. 6084 1003–1007, [https://www.science.org/doi/pdf/10.1126/science.1222360].

[18] N. Read and D. Green, *Paired states of fermions in two dimensions with breaking of parity and time-reversal symmetries and the fractional quantum hall effect*, *Phys. Rev. B* **61** (Apr, 2000) 10267–10297.

[19] L. Fu and C. L. Kane, *Superconducting proximity effect and majorana fermions at the surface of a topological insulator*, *Phys. Rev. Lett.* **100** (Mar, 2008) 096407.

[20] J. D. Sau, R. M. Lutchyn, S. Tewari, and S. Das Sarma, *Generic new platform for topological quantum computation using semiconductor heterostructures*, *Phys. Rev. Lett.* **104** (Jan, 2010) 040502.

[21] R. M. Lutchyn, J. D. Sau, and S. Das Sarma, *Majorana fermions and a topological phase transition in semiconductor-superconductor heterostructures*, *Phys. Rev. Lett.* **105** (Aug, 2010) 077001.

[22] Y. Oreg, G. Refael, and F. von Oppen, *Helical liquids and majorana bound states in quantum wires*, *Phys. Rev. Lett.* **105** (Oct, 2010) 177002.

[23] K. O. H., *The superconductivity of mercury*, *Comm. Phys. Lab. Univ. Leiden* **122** (1911) 122–124.

[24] R. P. Feynman, R. B. Leighton, and M. Sands, *The Feynman lectures on physics: The Definitive Edition (Vol. 3).* Pearson, 2009.

[25] P. Krantz, M. Kjaergaard, F. Yan, T. P. Orlando, S. Gustavsson, and W. D. Oliver, *A quantum engineer's guide to superconducting qubits*, *Applied Physics Reviews* **6** (June, 2019).

[26] B. Josephson, *Possible new effects in superconductive tunnelling*, *Physics Letters* **1** (1962), no. 7 251–253.

[27] B. D. JOSEPHSON, *Coupled superconductors*, *Rev. Mod. Phys.* **36** (Jan, 1964) 216–220.

[28] A. P. M. Place, L. V. H. Rodgers, P. Mundada, B. M. Smitham, M. Fitzpatrick, Z. Leng, A. Premkumar, J. Bryon, A. Vrajitoarea, S. Sussman, G. Cheng, T. Madhavan, H. K. Babla, X. H. Le, Y. Gang, B. Jäck, A. Gyenis, N. Yao, R. J. Cava, N. P. de Leon, and A. A. Houck, *New material platform for superconducting transmon qubits with coherence times exceeding 0.3 milliseconds*, *Nature Communications* **12** (Mar., 2021).

[29] C. Wang, X. Li, H. Xu, Z. Li, J. Wang, Z. Yang, Z. Mi, X. Liang, T. Su, C. Yang, G. Wang, W. Wang, Y. Li, M. Chen, C. Li, K. Linghu, J. Han, Y. Zhang, Y. Feng, Y. Song, T. Ma, J. Zhang, R. Wang, P. Zhao, W. Liu, G. Xue, Y. Jin, and H. Yu, *Towards practical quantum computers: transmon qubit with a lifetime approaching 0.5 milliseconds*, *npj Quantum Information* **8** (Jan., 2022).

[30] T. Schallenberg, C. Schumacher, and W. Faschinger, *In situ structuring during mbe regrowth with shadow masks*, *Physica E: Low-dimensional Systems and Nanostructures* **13** (2002), no. 2 1212–1215.

[31] Y. Luo, L. Zeng, W. Lin, B. Yang, M. Tamargo, Y. Strzhemechny, and S. Schwarz, *In situ device processing using shadow mask selective area epitaxy and in situ metallization*, *Journal of Electronic Materials* **29** (01, 2000) 598–602.

[32] C. Yang and J. Pham, *Characteristic study of silicon nitride films deposited by lpcvd and pecvd*, *Silicon* **10** (11, 2018).

[33] M. Barcellona, O. Samperi, D. Russo, A. Battaglia, D. Fischer, and M. E. Fragalà, *Differences in hf wet etching resistance of pecvd sinx:h thin films*, *Materials Chemistry and Physics* **306** (2023) 128023.

[34] D. P. Seraphim and R. A. Connell, *Resistance transitions in superconducting tantalum*, *Phys. Rev.* **116** (Nov, 1959) 606–612.

[35] B. Cornelius, S. Treivish, Y. Rosenthal, and M. Pecht, *The phenomenon of tin pest: A review*, *Microelectronics Reliability* **79** (2017) 175–192.

[36] N. Si, Q. Yao, Y. Jiang, H. Li, D. Zhou, Q. Ji, H. Huang, H. Li, and T. Niu, *Recent advances in tin: From two-dimensional quantum spin hall insulator to bulk dirac semimetal*, *The Journal of Physical Chemistry Letters* **XXXX** (01, 2020).

[37] S. Groves and W. Paul, *Band structure of gray tin*, *Phys. Rev. Lett.* **11** (Sep, 1963) 194–196.

[38] R. Farrow, D. Robertson, G. Williams, A. Cullis, G. Jones, I. Young, and P. Dennis, *The growth of metastable, heteroepitaxial films of -sn by metal beam epitaxy*, *Journal of Crystal Growth* **54** (1981), no. 3 507–518.

[39] L. D. Anh, K. Takase, T. Chiba, Y. Kota, K. Takiguchi, and M. Tanaka, *Elemental topological dirac semimetal -sn with high quantum mobility*, *Advanced Materials* **33** (2021), no. 51 2104645, [https://onlinelibrary.wiley.com/doi/pdf/10.1002/adma.202104645].

[40] Y. Ohtsubo, P. Le Fèvre, F. m. c. Bertran, and A. Taleb-Ibrahimi, *Dirac cone with helical spin polarization in ultrathin α-sn(001) films*, *Phys. Rev. Lett.* **111** (Nov, 2013) 216401.

[41] G. J. de Coster, P. A. Folkes, P. J. Taylor, and O. A. Vail, *Effects of orientation and strain on the topological characteristics of cdte/α-sn quantum wells*, *Phys. Rev. B* **98** (Sep, 2018) 115153.

[42] A. Barfuss, L. Dudy, M. R. Scholz, H. Roth, P. Höpfner, C. Blumenstein, G. Landolt, J. H. Dil, N. C. Plumb, M. Radovic, A. Bostwick, E. Rotenberg, A. Fleszar, G. Bihlmayer, D. Wortmann, G. Li, W. Hanke, R. Claessen, and J. Schäfer, *Elemental topological insulator with tunable fermi level: Strained α-sn on insb(001)*, *Phys. Rev. Lett.* **111** (Oct, 2013) 157205.

[43] V. A. Rogalev, F. Reis, F. Adler, M. Bauernfeind, J. Erhardt, A. Kowalewski, M. R. Scholz, L. Dudy, L. B. Duffy, T. Hesjedal, M. Hoesch, G. Bihlmayer, J. Schäfer, and R. Claessen, *Tailoring the topological surface state in ultrathin α-sn(111) films*, *Phys. Rev. B* **100** (Dec, 2019) 245144.

[44] C.-Z. Xu, Y.-H. Chan, Y. Chen, P. Chen, X. Wang, C. Dejoie, M.-H. Wong, J. A. Hlevyack, H. Ryu, H.-Y. Kee, N. Tamura, M.-Y. Chou, Z. Hussain, S.-K. Mo, and T.-C. Chiang, *Elemental topological dirac semimetal: α-sn on insb(111)*, *Phys. Rev. Lett.* **118** (Apr, 2017) 146402.

[45] R. Wagner and A. Ewald, *Free carrier reflectivity of gray tin single crystals*, *Journal of Physics and Chemistry of Solids* **32** (1971), no. 3 697–707.

[46] I. Madarevic, U. Thupakula, G. Lippertz, N. Claessens, P.-C. Lin, H. Bana, S. Gonzalez, G. Di Santo, L. Petaccia, M. N. Nair, L. M. Pereira, C. Van Haesendonck, and M. J. Van Bael, *Structural and electronic properties of the pure and stable elemental 3D topological Dirac semimetal -Sn*, *APL Materials* **8** (03, 2020) 031114, [https://pubs.aip.org/aip/apm/article-pdf/doi/10.1063/1.5142841/14563855/031114_1_online.pdf].

[47] E. Magnano, C. Cepek, S. Gardonio, B. Allieri, I. Baek, E. Vescovo, L. Roca, J. Avila, M. G. Betti, C. Mariani, and M. Sancrotti, *Sn on insb(100)–c(2×8):*

growth morphology and electronic structure, *Journal of Electron Spectroscopy and Related Phenomena* **127** (2002), no. 1 29–35. IWASES 5 Special Issue.

[48] J. Ren, L. Fu, G. Bian, M. Wong, T. Wang, G. Zha, W. Jie, T. Miller, M. Z. Hasan, and T.-C. Chiang, *Spectroscopic studies of* CdTe(111) *bulk and surface electronic structure*, *Phys. Rev. B* **91** (Jun, 2015) 235303.

[49] O. Vail, A. Chang, S. D. Harrington, P. A. Folkes, P. J. Taylor, B. M. Nichols, C. J. Palmstrøm, and G. J. de Coster, *Gated magnetotransport in α-sn thin films on cdte*, *Journal of Electronic Materials* **50** (2021) 6329 – 6336.

[50] H. Huang and F. Liu, *Tensile strained gray tin: Dirac semimetal for observing negative magnetoresistance with shubnikov–de haas oscillations*, *Phys. Rev. B* **95** (May, 2017) 201101.

[51] S. Küfner, M. Fitzner, and F. Bechstedt, *Topological α-sn surface states versus film thickness and strain*, *Phys. Rev. B* **90** (Sep, 2014) 125312.

[52] J. T. Dong, H. S. Inbar, M. Pendharkar, T. A. J. van Schijndel, E. C. Young, C. P. Dempsey, and C. J. Palmstrøm, *Electronic structure of insb (001), (110), and (111)b surfaces*, *Journal of Vacuum Science amp; Technology B* **41** (May, 2023).

[53] W. Liu and M. Santos, *Surface reconstructions of insb(001) during molecular beam epitaxy*, *Surface Science* **319** (1994), no. 1 172–183.

[54] A. N. Engel, C. P. Dempsey, H. S. Inbar, J. T. Dong, S. Nishihaya, Y. Chang, A. V. Fedorov, M. Hashimoto, D. Lu, and C. J. Palmstrøm, *Growth and characterization of α-sn thin films on in- and sb-rich reconstructions of insb(001)*, *Phys. Rev. Mater.* **8** (Apr, 2024) 044202.

[55] R. Steadman, *Materials science*, *Physics Education* **5** (mar, 1970) 70.

[56] M. Jafarian, F. Gobal, I. Danaee, R. Biabani, and M. Mahjani, *Electrochemical studies of the pitting corrosion of tin in citric acid solution containing cl*, *Electrochimica Acta* **53** (2008), no. 13 4528–4536.

[57] Y. Ding, H. Song, J. Huang, J. Yao, Y. Gu, L. Wei, Y. Deng, H. Yuan, H. Lu, and Y.-F. Chen, *Large magnetoresistance observed in α-sn/insb heterostructures*, 2020.

[58] S. Ishida, *Magnetic freeze-out and impurity band conduction in n-insb*, *Physica E: Low-dimensional Systems and Nanostructures* **18** (2003), no. 1 294–295. 23rd International Conference on Low Temperature Physics (LT23).

[59] M. von Ortenberg and G. Landwehr, *Magnetic freeze-out in indiumantimonide*, *Solid State Communications* **8** (1970), no. 23 1955–1958.